Going Deeper into Laser Damage: Experiments and Methods for Characterizing Materials in High Power Laser Systems

A THESIS
SUBMITTED TO THE FACULTY OF THE GRADUATE SCHOOL
OF THE UNIVERSITY OF MINNESOTA
BY

Lucas Nathan Taylor

IN PARTIAL FULFILLMENT OF THE REQUIREMENTS
FOR THE DEGREE OF
Doctor of Philosophy

Joseph Talghader

May, 2016

Acknowledgements

While it's difficult to acknowledge everyone who helped, certain individuals uniquely contributed to this work's success. Engaging discussions with Bradley Tiffany and Jordan Burch provided inspiration and insight into the optical system design. Andrew Brown provided essential aid in the laser damage experiment design as well as execution. Kyle Olson provided vital inspiration and discussion of the thermal models. Phil Armstrong provided excellent discussions, humor and common sense for every aspect of this work. Wing Chan and Merlin Mah provided encouragement and general strategic planning of the experiments and data analysis methods. Sangho Kim, Nick Gabriel, Anand Gawarikar and Ryan Shea provided senior encouragement. Sara Rothwell, Joe Stansberry, Jon Lake, Yu-Jen Lee and Tirtha Mitra provided helpful discussions and helped make the office a fun and supportive environment. Outside of the office, Justin Taylor, Zach Taylor, Katie Taylor, Matt Decuir, Marijke Decuir, John Koester, Freya Koester, Josh Beebe, Pat Grady, Randi Shandroski, Peter Martin, Tom Johnson, Taylor Baldry, Regan Smith, Tim Lovett, Krisi Johnson, Gabe Jorgenson (and everyone I missed!) were the most supportive friends anyone could want. My parents Jeff and Lynn Taylor provided essential support. Janet and Gordy Spielman provided support. Liz Spielman was a supportive friend and everything else. Without her I would have never made it. Nick Moen, Matt Gemlo and Patrick Schiavone were incredibly supportive and are great band-mates. Kiki was a great cat and kept me warm many late nights of writing. The baristas at Five Watt coffee provided the humor and caffeine needed to get through some of the more difficult tasks in this work.

Last, but not least, Joey Talghader was the advisor and tireless supporter of this work. He provided essential direction, was patient through missteps and frustrations and welcomed my successes.

Dedication

This work is dedicated to Liz, the most wonderful person in my life.

Abstract

Laser damage is a primary limiting factor to the design of high-power laser systems. This is true for short-pulse systems as well as long-pulse and continuous-wave (CW) systems. Unlike short-pulse laser damage, CW laser damage has been much less studied. This work comprises a background of laser damage and laser heating theory, a CW laser damage experiment and an imaging technique for monitoring laser heating. The damage experiment was performed on 100 nm thick hafnia coatings deposited on fused silica. Uniformly grown films were compared to hafnia-alumina nanolaminates. While the nanolaminates are known to perform better for 1 ns pulses, we found they had worse laser damage performance in the CW regime. We found the nanolaminates reduced crystallinity. The polycrystalline uniform films are thought to have increased absorption. We measured the thermal conductivity of the nanolaminates to be approximately 1/2 that of the uniform films. A theoretical model including the absorption and thermal conductivity of the nanolaminate and uniform film agreed with the experimental data for 1 ns pulses and CW tests. During laser damage experiments, anomalous damage morphologies were observed that we were unable to explain with theoretical techniques. We then developed an experimental method to observe high-speed laser damage events at the ms time-scale. We imaged laser heating and compared it to a theoretical model with good agreement. Our measurement method captured image data from a Mach-Zender interferometer that had do be processed ex-situ. We desired a system capable of providing real-time thermal data. We developed an image processing technique at least 66 times faster than the original method.

Contents

List of Tables

List of Figures

Chapter 1

Introduction

This thesis comprises the following work: a laser damage experiment on two types of optical coating materials; a high-speed imaging experiment motivated by unique morphologies observed in the first study; a fast image processing technique motivated by applying the high-speed imaging system to capture thermal data in real-time. The work includes a chapter providing a theoretical background for laser damage. Background for the other physical mechanisms are developed as they are encountered in the thesis.

1.1 Motivation

The progress of science can be measured by the improvement of theoretical laws and experimental accomplishments to better understand our universe. The work of engineers is to apply scientific advances to solve problems, and often to influence new scientific progress in return. In addition to these basic functions, scientists and engineers are responsible for improving the philosophies and paradigms used to understand nature. These paradigms are used to orient research programs and design solutions to physical problems. One of the most iconic paradigms of the last century has been the invention of the laser. Research programs devoted to the understanding of laser physics are common at every major university. However, a problem present during even the earliest laser experiments has been the high concentration of power a laser experiment may produce [1]. The laser damage resistance of optical components remains a limiting factor to high power laser system design [2]. A practical example of this is in high-energy pulsed laser

systems and high-power continuous-wave (CW) laser systems. The primary limitation of many high-power systems is the laser damage threshold of the consituent optics. These are the mirrors, lenses and diffractive optical elements essential in any laser system. The total system will only be as strong as the weakest element. Therefore, much work has been put into laser system design to reduce the power load on constituent elements. For example, systems are designed to have a maximum beam diameter (and thus larger optics) everywhere except where power is needed. Larger beam diameters have reduced optical power density. Conversely, the larger optics required may have more defects. Because of this, much work has been put into reducing the absorption of the constituent elements. This has been done by increasing the cleanliness of nanofabrication processing, by improving deposition methods and by designing optical devices with reduced absorption[2, 3, 4, 5]. At the same time more has been learned about the materials with which optical devices are designed. Certain materials may be preferrable in certain regimes due to larger electronic bandgaps, reduced defect count and high thermal conductivity [6, 2]. This results in a multi-tiered material and system design problem. Nowhere is this more apparent than in the integration of metamaterials into optical systems. The concept of a metamaterial is an extension of our concept of a material itself: a collection of atoms or molecules forming a physical entity with associated properties, hazards and uses. Despite the apparently broad nomenclature, the term metamaterial is typically applied to materials characterized by their wave response: electromagnetic or acoustic. The term metamaterial first gained prominence in connection to a material invented by Pendry and Smith [7, 8, 9, 10, 11, 12, 13, 14]. Their work was, in turn, a response to an obscure observation by a Russian scientist, almost buried by time[15]. Pendry and Smith's metamaterial was designed to adjust the refractive index by creating an array of small atom-like circuits. It was designed to function for invisible microwave radiation (much like the predecessor to the laser, the microwave maser). The circuit cells they designed were required to be much smaller than the wavelength of the operating radiation. The interesting part of this material was that it had a negative index of refraction. This has lots of implications, including that a beam of light will bend the wrong way when it refracts through the material, and that the material will amplify scattered evanescent waves allowing the material to have

resolution below the typical diffraction limits. Needless to say, metamaterials are a useful concept, not just for negative index, but for arbitrary index and new types of optical elements. Metamaterials have been the subject of much research and many advances in recent years. However, one area where metamaterials are still limited is in the high power regime. This is because they tend to absorb large amounts of energy and dissipate it poorly leading to undesirable material changes. Metamaterials are non-homogeneous by design. In addition, the current processes used to create metamaterials are very immature and low defect counts are largely desirable only to the extent that proof-of-concept experiments are possible. Therefore, most metamaterials produced by research programs are not suitable for high power systems. Nevertheless, the basic metamaterial concepts are still of use. Metamaterials may be specifically useful to high-power systems in many cases [16, 17, 18, 19]. Therefore, an understanding of some of the roadblocks toward high-power metamaterials is very useful.

Power density has been a problem for the electronics industry as well [20]. As electronic and photonic systems become more complex and transmit more power, the amount of power that inevitable is lost to heat increases. Therefore, reducing loss and increasing thermal dissipation is of paramount importance.

In order to better understand physical phenomena, new experiemental methods are developed. Fortunately, the experiemental methods developed in the last century have provided us with an almost-complete picture of the building blocks of nature. Methods to analyze light, matter and information have been developed. Specifically, optical methods provide a fast and precise means of measuring physical quantities. For example, grating spectrometers can give us the amount of light reflected and transmitted by a material at each wavelength of light. From this the optical absorption can be estimated. However, most grating spectrometers do not have enough precision to measure small absorptions. Therefore, new techniques such as photothermal common-path interferometry (PCI) have been developed to measure the small absorptions important in high-power systems [21, 22, 23, 24]. Another optical technique which has seen continual improvement is the field of microscopy. The measurement of microscopic quantities is becoming ever more quantitiative and precise. Techniques are being developed to overcome the limits of the light used to measure material properties. Furthermore, techniques to recover the optical phase of the microscopic sample have been developed.

This allows a wealth of new material properties, including volume changes and temperature to be studied. While physical techniques, such as atomic force microscopy or high-energy optical scattering, such as x-ray diffraction can probe the more fundamental material properties, optical techniques are becoming more and more improved. For example, high-speed optical tests have been able to capture electronic events in optical materials down to the femtosecond time-scales during laser damage testing [25]. Results from these experiements show that we have the experimental tools to analyze the complex reactions in high-power media.

High power, in this work, refers to the high radiation power encountered in laser systems. This includes high electric and magnetic fields (sometimes very high) and long on-times. Much of the laser damage literature concerns high-energy, short pulse laser damage. The laser breakdown theory and experiments have been well developed since the early 1970s [26]. Conversely, relatively few studies have been performed on long-pulse and CW systems [27, 28]. In these systems, the laser intensity may be lower, but the dwell time is longer. Therefore, the materials that comprise the high power system must maintain their characteristics for the duration that they conduct or transmit power. These materials are often required to be largely homogeneous and have low defect densities to reduce optical absorption and increase energy dissipation.

1.2 Outline

In this work, the theoretical and experimental tools needed to study CW laser damage in the thermal regime are developed. This work concerns experiments and techniques which provide a greater understanding of how optical materials and devices behave in high power, long-pulse laser systems. The work is outlined below:

- Chapter 2 covers the physical mechanisms leading up to laser damage in optical materials. It begins with fundamental treatments for short pulse optical irradiation and continues to treat the additional mechanisms and issues that occur for long-pulse and CW laser damage.

- Chapter 3 describes an experiment to differentiate between nanolaminate films and uniformly-grown films during high power laser damage testing. Nanolaminate

films had comparable optical absorption, higher crystalline disorder, lower thermal conductivity and had reduced laser damage resistance.

- Chapter 4 describes an instrument designed to capture thermal waves during high power laser testing. This instrument could be used to characterize metamaterial performance. We measured material temperature changes during laser heating evens and found experimental data matched very well with theoretical thermal models.

- Chapter 5 describes an improved method for fast thermal data retrieval from the simple optical system outlined in Chapter 4. By sub-sampling the interference images, thermal data can be recovered as fast as it is recorded.

- Chapter 6 presents a final discussion of the analyses presented in the thesis.

Chapter 2

Laser Damage in Dielectric Optical Materials

2.1 Introduction

Laser damage is the process by which light-matter interactions irreversibly change an optical material. What this means is often dependent on the system under study. Catastrophic damage includes melting, cracking, ablation and mass ejection [6, 2]. More subtle effects may occur in practice, such as the Kerr effect and thermo-optic effect which do not cause catastrophic damage, but may impact system performance. The purpose of this chapter is to explore how high-power laser radiation interacts with optical materials. This discussion will be focus on optical oxides illuminated by laser wavelengths from visible to near-IR. These oxides include SiO_2, HfO_2, TiO_2, Ta_2O_5 and Al_2O_3. These materials have bandgaps from 4-9 eV, while the laser radiation has photon energies from 0.1 to 3 eV. The chapter will briefly introduce the terminology and units of laser damage as well as an overview of the optical materials considered.

This chapter will consider two main types of laser damage. The first type is laser damage due to high field effects. These high field effects include multiphoton absorption and impact ionization. These effects are important because they are present in any material, regardless of defects [2]. However, typically only fs-ps laser systems produce fields high enough for these effects to be appreciable. The second type of laser damage covered is due to long-pulse heating of optical materials. These heating effects become

important for 10 ps pulse lengths and greater [29]. This section will include laser heating models, melting, thermal expansion and the thermo-optic effect. Laser heating, thermal expansion and the thermo-optic effect are utilized to quantify laser heating in Chapters 4 and 5. The chapter will close with a comparison of ns and CW laser damage of an amorphous film with low thermal conductivity and low optical absorption and a polycrystalline film with high thermal conductivity and higher optical absorption. This comparison provides a theoretical backdrop for the first experiment, in Chapter 3.

2.1.1 Laser parameters in laser damage

Before discussing physical mechanisms, the terminology of laser damage should be discussed. Laser-induced damage threshold (LIDT) is typically defined as the highest laser power a material or device can withstand before breaking down. The term laser damage resistance is also used and connotes the same idea. Ideally, the concept of laser damage threshold assumes that a critical laser power can be determined for any given optical material. The laser damage threshold is often given in terms of either optical intensity, in W/m^2, or fluence, in J/m^2 [2]. For pulsed lasers, the two quantities are approximately related by:

$$I_D = \frac{F_D}{\tau} \tag{2.1}$$

where I_D is the threshold intensity in W/m^2 and F_D is the threshold fluence in J/m^2. Here τ is the beam pulse width in seconds. Implicit in these terms is the beam waist w. The total energy of the pulse in joules (E_p) is equal to the fluence muliplied by the beam area: $E_p = \pi w^2 F_D$. Short pulse lasers are often defined in terms of their total pulse energy in joules. However, damage mechanisms for short pulse lasers are often driven by the peak intensity [30, 26, 31]. Equation 2.1 can be used to estimate the peak pulse intensity given the laser pulse energy and beam waist.

Table 2.1 summarizes some of the mechanisms and dependencies of laser damage in short and long pulse regimes. The table presents damage mechanisms in a simplified picture. For example, defect absorption would certainly be a primary mechanism in every regime. However, in the short pulse regime non-linear effects become very imporatant even in the absence of defects. These mechanisms will be explored further in the

sections to follow. The table also summarizes current scaling laws for pulselength (τ) and pulsewidth (w). In the nanosecond regime, a $\tau^{1/2}$ law for LIDT has been observed for a number of studies and theoretical works [32, 33, 34, 6, 35, 36]. It deviates from the linear behavior predicted from 2.1 and is attributed to pulse-heating of excited carriers. In the fs regime, deviation from the $\tau^{1/2}$ law has been observed in at least two major studies [34, 6]. In the CW regime laser damage is dependent on laser heating of the optical material [37]. The table also includes example values of laser damage threshold for silicon dioxide given in the units appropriate to the regime.

Table 2.1: Laser Damage Regimes

Term	short-pulse fs-ps	ps-ns	long pulse ns-CW
Primary mechanism	Non-linear absorption [34]	Defect absorption & heating [34]	Heating [37]
Pulselength dependence, τ (s)	$\approx \tau^{-1}$ [34]	$\tau^{1/2}$ [34]	$\tau^{1/2}$ [37]
Pulsewidth dependence, w (m)	- [38]	w^{-2} [38]	w^{-2}-w^{-1} [38]
SiO_2 LIDT	300 mJ/cm^2 [39][a]	2 J/cm^2 [40][b]	>10 MW/cm^2 [c]

[a] $\lambda = 800$ nm, τ =120 fs, $w = 160$ μm, fused silica fiber

[b] $\lambda = 1064$ nm, τ =23 ns, $w = 15$ μm, fused silica substrate

[c] unpublished data, $\lambda = 1.064$ μm, τ >1 ms, $w = 1$ mm, fused silica substrate

For the case of CW lasers, the pulse length is infinite, although a finite dwell time is used. In this case, laser systems are defined by their power output in watts. Laser damage mechanisms are typically thermal. Therefore the laser damage threshold is often a stronger function of total absorbed power rather than power density [38].

There are many laser systems in the visible-near IR wavelength range that may produce damage-inducing radiation. In this work we are primarily interested in 1064 nm light produced by an Nd:YAG laser. Our experimental system, detailed in Sections 3.4 and 4.2, was capable of producing 1064 nm radiation at 300 W CW or 180 W avg power 100 ns Q-switched pulses at a 5 kHz repetition rate [41]. Other systems mentioned in this chapter include multiple-kW 1064 nm CW fiber laser systems [42, 43] and 800 nm Ti:Sapphire systems capable of producing μJ pulses in the sub-ns range [44, 45, 46].

Next a cursory overview of the materials under consideration will be presented.

2.1.2 Dielectric materials under consideration

In this work we are primarily concerned with the laser heating and damage of dielectric oxides. As mentioned previously they include SiO_2, HfO_2, TiO_2, Ta_2O_5 and Al_2O_3 with bandgaps from 4-9 eV. SiO_2 is typically a substrate material, while the other materials are typically only present in film form. In the visible-near IR spectrum, these materials have very low bulk absorption – in the ppb range. Processing defects, surface states, film properties and contamination may increase the linear absorption, and thus reduce the laser damage threshold. These materials also tend to have relatively low thermal conductivity compared to crystalline silicon. It should be noted that the detailed electronic structure of these materials have not been very well characterized. Amorphous materials in general are a subject of active research. Table 2.2 summarizes common values of bandgap (E_g), thermal conductivity (k) and LIDT (F_D) for the materials under consideration.

Table 2.2: Dielectric Materials under consideration

Material	E_g (eV)	k (W m^{-1} K^{-1})	F_D J/cm^2
SiO_2	8.3	1.61[a]	6[d]
Al_2O_3	6.5	2.59[a]	3.5[d]
HfO_2	5.1	1.72[a]	2[d]
Ta_2O_5	3.8	2.8[b]	1.1[d]
TiO_2	3.3	1.6[c]	0.9[d]

[a] 100 nm ALD-deposited film, after [47]

[b] 2 μm e-beam evaporated film, after [48]

[c] 100 nm RF-sputtered film, after [49]

[d] 1 ps, 800 nm irradiation, after [50]

With the laser parameters and optical materials in mind, we will look at the physical factors that go into laser damage. First, we will look at how to theoretically approach a laser damage threshold for pulsed laser radiation.

2.2 Short pulse laser damage

The point of this section is to communicate the fundamental limit of any material to withstand very high intensity laser irradiation. Defects and surface absorption will certainly lower this limit, but this limit is present regardless. The formalism used to describe very high intensity light-matter interactions for transparent media is through multiphoton absorption, tunneling and avalanche ionization [26, 51, 34, 6, 50, 36]. The presentation in this section follows the current theoretical understanding of short pulse damage [50, 36]. For pulses in the fs range, the bulk of the lattice may not heat much at all, while the surface may experience precise material removal [29, 52]. The absorbed energy can remove a very small volume of material without much thermal spread or thermal effects such as cracking or melting. This has been exploited for precise laser machining. In terms of damage threshold, irreversible changes occur when the excited carriers are able to transfer a significant amount of energy to the lattice. One metric for laser damage threshold is when the total carrier number reaches a critical plasma density [34, 53, 50], such that the plasma frequency is equal to the irradiant laser frequency: $\omega_p = \omega$, where $\omega_p^2 = (Ne^2)/(m\epsilon_0)$. N_{cr}= 10^{22} cm^{-3} is a value for 800 nm Ti:Sapphire laser systems irradiant on SiO_2 [50]. The common theory is that electron-hole pairs are generated through non-linear absorption. These carriers are then heated and transfer their energy to the lattice. The generation of electrons by non-linear ionization can be described by a simple rate equation [50]:

$$\frac{dN}{dt} = \alpha N(t)I(t) + \beta_m \left(I(t)\right)^m - \frac{N(t)}{\tau} \tag{2.2}$$

Here, m is the number of photons required to excite a carrier above the bandgap (typically 4-8 for the materials and wavelengths we are considering), N is the number of free electrons generated, I is the intensity of the short pulse laser, α is a impact ionization parameter, β_m is a multiphoton absorption parameter and τ is the carrier recombination time. This equation includes three terms on the right-hand-site.

The first, $\alpha N(t)I(t)$ takes into account impact ionization. This is the generation of carriers by existing carriers accelerated by the high electric field of the laser. In a simplified picture, these accelerated carriers may collide with valence electrons and produce an additional free electron-hole pair. It should be noted that impact ionization

is a secondary effect that requires free-carriers be initially present. It has been theorized that these carriers may be supplied by defects or by multiphoton absorption.

The second term in Equation 2.2 is the multiphoton ionization term. Multiphoton ionization is the process by which more than one photon may interact with the same electron and supply it with enough energy to transition to a higher state, as allowed by selection rules. The number of photons required is dependent on the bandgap energy of the material and the photon energy of the incident laser radiation. Since our discussion is limited to materials with bandgaps in the 4-9 eV range, and photon energies near 1 eV, we are considering 4 to 9 photon transitions. Typically lower photon-number transitions have a higher β_m. Also, it has been shown theoretically that the transition rate is highest for an integer multiple of the photon energy that is equal to or slightly less than the bandgap [54]. The final term in Equation 2.2 is the electron-hole recombination rate. This reduces the number of carriers present. Typical recombination times for the optical materials considered are greater than 200 fs [50]. This term can be neglected for pulselengths shorter than the recombination time. Equations like this have been very successful at predicting laser damage for short pulse laser radiation. It is worth going into greater depth into each mechanism in terms of material and laser properties.

Depending on the values used, either impact ionization or multiphoton absorption may be the dominant mechanism. Figure 2.1 shows the relative contribution of impact ionization at short and longer pulse widths, using values for α and β_6 (for 800 nm irradiation and 8 eV SiO_2 bandgap) from [50]. The relative contributions of impact ionization and multiphoton absorption are still in dispute [51, 36]. These mechanisms will be described further in the next sections.

2.2.1 Multiphoton ionization

In the linear regime, photons with energy less than the bandgap, and with energy above the vibrational absorption bands are not absorbed by optical media. However, extremely intense light may have an appreciable probability of exciting an electron above the bandgap by combining the energy of multiple photons. The fundamental theory of this interaction was described by Keldysh and has been summarized elsewhere [55]. Keldysh formulated the interaction by a first-order perturbation theory, despite the number of photons involved, by including a field term in the electronic wavefunction.

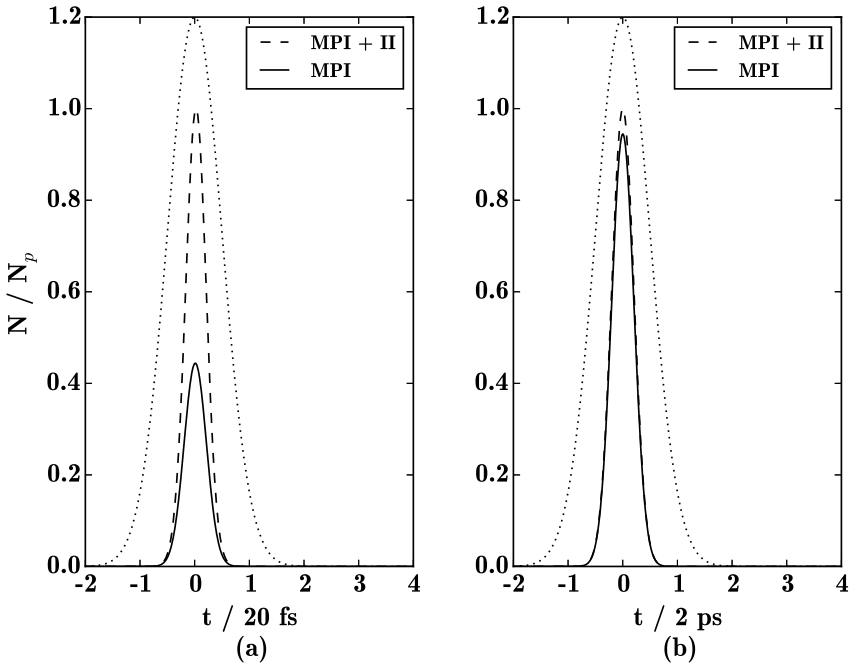

Figure 2.1: Relative contribution of impact ionization (II) and multiphoton ionization (MPI) to carrier generation in (a) fs and (b) ps regimes. Calculation made for 800 nm, 20 nJ, 20 μm laser light incident on SiO_2, after [50]

While complicated, his work has been approximated for a short-pulse (relatively) weak-interaction in [50]. In the simple picture in Figure 2.2, photons can add their respective energies together to give an electron enough energy to reach the next allowed state. This figure shows a 6 photon process whereby 6 photons combine energy to create an electron hole pair in a material with a bandgap $E_g = E_c - E_v$.

For light from a 1064 nm Nd:YAG laser irradiated on a silica sample, 8 photons are needed to generate an electron-hole pair. Photons from the laser have an energy of 1.165 eV, while the silica bandgap is on the order of 8.9 eV. To calculate photon probabilities, a simplification of the full Keldysh formula for dielectrics can be used [50]:

$$\beta_m \approx \frac{\omega}{9\pi}\left(\frac{m_r\omega}{\hbar}\right)^{3/2}\left(\frac{e^2}{8\omega^2 m_r c\epsilon_0}\right)^m \frac{\exp(2m)}{(n_0 E_g)^m} \tag{2.3}$$

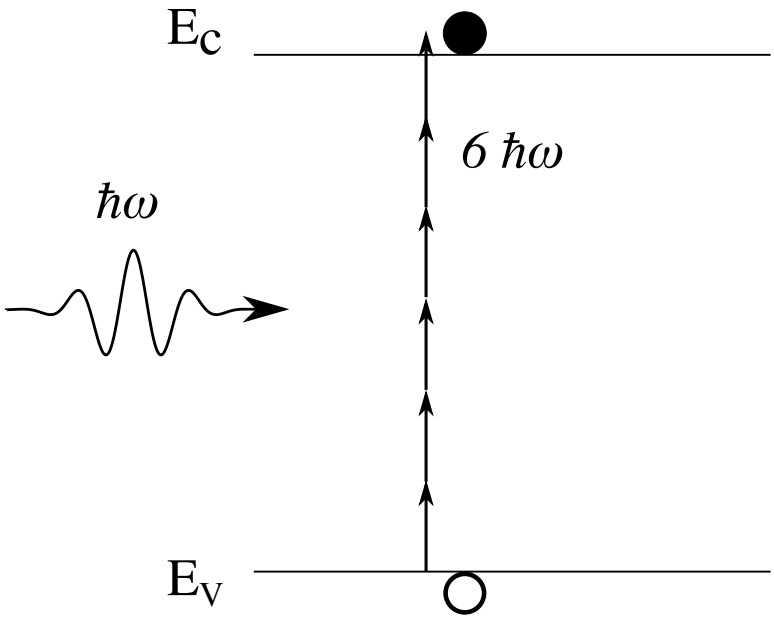

Figure 2.2: Multiphoton absorption depicted as a 6 photon event. 6 photons with energy $\hbar\omega$ combine to excite an electron-hole pair across a bandgap of $E_g = E_c - E_v$.

Here, ω is the angular frequency of the incident light, m is the number of photons needed, where $m = \text{mod}(E_g/\hbar\omega)$. The other parameters are m_r, the reduced mass, e the electron charge and c the speed of light in vacuum. The rate of electrons ionized by a multiphoton event is given by:

$$\left(\frac{dN}{dt}\right)_{MPI} = \beta_m I(t)^m \tag{2.4}$$

A table of values from Equations 2.3 and 2.4 for 1064 nm light with 1 mJ pulses and pulse time 1 fs, 1 ps, and 1 ns are given in Table 2.3, using material parameters from [50]

2.2.2 Impact ionization

Impact ionization is the process by which one carrier may gain enough energy to excite a second carrier to the conduction band. If conditions are right, this carrier multiplication process may result in a large number of carriers generated through avalanche. These

Table 2.3: Multiphoton carrier generation for 1064 nm 80 mJ irradiation.[a]

Material	E_g (eV)	m	$\tau_e(fs)$	β_m (cm^{2m-3} s^{m-1} J^{-m})	N_{fs} (cm^{-3})	N_{ps} (cm^{-3})	N_{ns} (cm^{-3})
SiO_2	8.3	8	220	8.2×10^{-103}	1.3×10^{34}	2.9×10^{11}	0
Al_2O_3	6.5	6	220	6.9×10^{-68}	1.7×10^{35}	3.9×10^{18}	3.9
HfO_2	5.1	5	1050	1.5×10^{-47}	4.7×10^{38}	5×10^{25}	5×10^{10}
Ta_2O_5	3.8	4	490	2.4×10^{-29}	9.4×10^{39}	4.6×10^{29}	4.6×10^{17}
TiO_2	3.3	3	120	4.1×10^{-13}	2×10^{39}	2.4×10^{31}	2.4×10^{22}

[a]after [50]

carriers heat the lattice as well, causing material breakdown. Figure 2.3 shows an electron in the conduction band being accelerated by a field. When the electron gains a bandgap's worth of energy it may collide with a valence electron, generating an electron-hole pair.

This process contributes an additional carrier generation term to the total free-carrier concentration in the material. This generation term is dependent on the bandgap as well as the field present in the material. From 2.2, the generation rate may be given by:

$$\left(\frac{dN}{dt}\right)_{II} = \alpha N(t) I(t) \tag{2.5}$$

Here, α is defined as the avalanche coefficient. Over the history of laser damage studies, impact ionization was first considered a candidate to explain many of the laser damage phenomena observed in a wide variety of materials. It certainly explained the sharp threshold encountered in the LIDT. In addition, models based on impact ionization had success modeling some of the pulselength dependence of the LIDT [34, 6]. However, impact ionization is based on a theory developed for DC fields [2, 51, 36]. Optical fields rapidly change in time. For example, a 800 nm optical wave has a field component that may be instantaneously on the order of the DC breakdown field, but will shift in the opposite direction within 2.6 fs. This switching field does not transfer any average momentum to the free carrier in the material. This formulation implies impact ionization is a rather unlikely mechanism for high frequency optical fields. In addition,

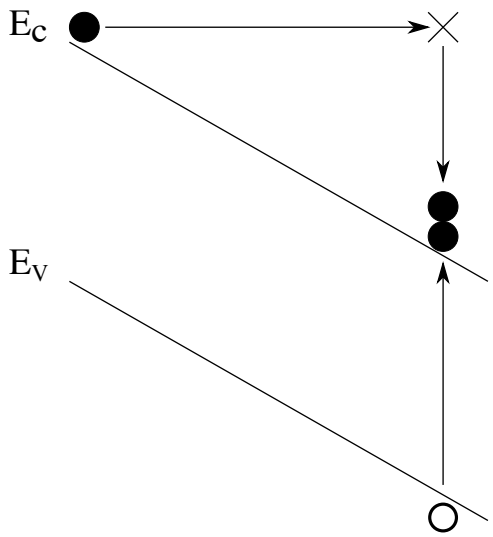

Figure 2.3: Impact ionization depicted as an electron in a DC field in the conduction band of an optical exciting a second electron-hole pair. In this simplified picture, field must be strong enough such that an electron can gain at least a bandgap's worth of energy. This schematic neglects the conservation of momentum in the scattering process.

from this perspective, laser damage should be more likely as the optical frequency decreases, i.e. the field points in the same direction longer. Experimentally, the opposite has been found to be true [51, 50, 36], leading the multiphoton ionization theory to gain support. Therefore, current theory of laser damage is that impact ionization is only appreciable during laser pulses with extremely high fields.

2.3 Laser Heating of Dielectric Materials

For laser pulses on the order of the thermal diffusion time, heating of optical materials is important. Even short pulse laser systems require thermal considerations if there are multiple pulses. The spatial area and temporal length of a laser pulse determines the thermal effects to a large extent. The region of the sample where the energy is absorbed and the time of the absorption determine whether or not the absorbed energy will spread appreciably during the laser test. The thermal diffusion time is proportional

to the pulse area by the diffusivity coefficient, D:

$$\tau = w^2/D \tag{2.6}$$

If the pulse time is longer than the absorbed area w^2 over the diffusivity coefficient D, then diffusion will occur during the laser test. In addition, if the area of the absorbed laser energy w^2 is much smaller than the diffusion area $D\tau$ for a given pulse length, then diffusion will occur more strongly. For a short pulse that deposits energy in a time much shorter than the diffusion time, the solution to the heat diffusion equation is given by a product solution in cylindrical coordinates [56, 37]:

$$\Delta T(r,z,t) = \frac{AE/\rho c}{2\pi^{3/2}\sqrt{Dt}w^2(t)} \exp\left[-\frac{r^2}{2w^2(t)}\right] \exp\left[-\frac{z^2}{4Dt}\right] \tag{2.7}$$

Here, E is the laser pulse energy, A is the material absorption coefficient, ρc is the thermal mass of the material and $w(t)$ is a time-dependent width given by:

$$w^2(t) = w_0^2 + 2Dt \tag{2.8}$$

Here, w_0 is the incident gaussian laser beam waist and D is the thermal diffusivity of the material. Equation 2.7 is valid for laser pulses much shorter than the thermal diffusion time for the initial beam waist, $\tau \ll w_0^2/D$. For a typical optical material with a diffusivity of 10^{-7} m^2/s, and a beam waist of 100 μm, this time is 100 ms, so a even a laser pulse length in the μs will still satisfy this requirement. The pulse spreads out in time in r and diffuses according to standard thermal diffusion in z. Of particular interest is the behavior at the center of the pulse. This shows how the peak temperature decays with time. For multiple pulses, if the next pulse arrives within this time, the temperature due to each pulse will accumulate over time. The center temperature is given by the following:

$$\Delta T(0,0,t) = \frac{AE/\rho c}{2\pi^{3/2}\sqrt{Dt}(w_0^2 + 2Dt)} \tag{2.9}$$

For pulse widths much greater than the thermal diffusion length, the temperature will decay as $t^{-1/2}$, whereas for pulse widths much less than the thermal diffusion length, the temperature will decay faster, as $t^{-3/2}$.

For pulse lengths on the order of the diffusion time or longer, the shorter-pulse solutions can be summed or integrated to give a true CW solution to thermal heating:

$$\Delta T(r,z,t) = \frac{1}{2\pi^{3/2}\rho c}\int \frac{A(t-t')P(t-t')}{\sqrt{Dt}w^2(t)} \exp\left[-\frac{r^2}{2w^2(t)}\right] \exp\left[-\frac{z^2}{4Dt}\right]dt' \tag{2.10}$$

where here, absorption and laser power are given as time-dependent, $A(t)$ and $P(t)$ and are convolved with the thermal response. This is because each absorption event can be thought of as an infinitesimal pulse of energy $A(t)P(t)dt$ occuring at time t'. For linear absorption, with a unit step laser temporal profile, the equation simplifies to:

$$\Delta T(r,z,t) = \frac{AP_0}{2\pi^{3/2}\rho c}\int_0^t \frac{1}{\sqrt{Dt}w^2(t)} \exp\left[-\frac{r^2}{2w^2(t)}\right] \exp\left[-\frac{z^2}{4Dt}\right]dt' \tag{2.11}$$

Where P_0 is the height of the CW laser power unit step function. This shows that the increase in temperature is a function of linear absorption A as well as thermal properties dependent on the laser beam waist w_0 (in $w(t)$) and on time, and material diffusivity D. Equation 2.11 must be integrated to obtain the temperature of the CW laser heated sample at time t. This can be simplified if the peak temperature is considered instead of the full temperature distribution. The center of the temperature distribution is the hottest point and thus plays a central role in thermal damage. In this case, only the $\sqrt{Dt}w^2(t)$ term in the denominator ofthe integral is integrated. This results in an arctan function [57]:

$$\Delta T(0,0,t) = \frac{AP_0}{(2\pi)^{1/2}w_0 k} \arctan\left(\frac{\sqrt{2Dt}}{w_0}\right) \tag{2.12}$$

Here k is the thermal conductivity of the material (see, for example, Table **??**). This equation shows that, for a given beam waist w_0, the peak temperature is proportional to A/k, that is, the ratio of absorption to thermal conductivity. The temperature rise for a variety of pulsewidths is given in Figure 2.4.

Equation 2.12 can be approximated for short and long pulses. For short pulses, $t \ll w_0^2/(2D)$ and the peak temperature takes the following form:

$$\Delta T_{short}(0,0,t) \approx \frac{AP_0}{\pi^{3/2}w_0^2 k}\sqrt{Dt} \tag{2.13}$$

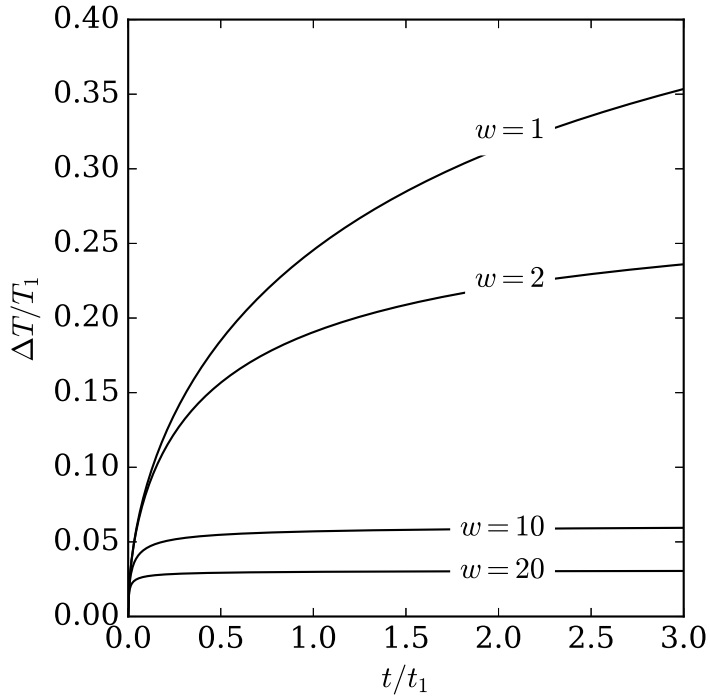

Figure 2.4: Temperature rise due to laser heating for a number of different beam waists, according to Equation 2.12. The peak temperature is $T_1 = AP/w_1k$ and the thermal time constant is $t_1 = w_1^2/D$. All plots are for identical laser and material parameters other than beam waist.

Here, the peak temperature is proportional to the absorbed power per unit area, AP_0/w_0^2, and rises as $t^{1/2}$. Conversely, for CW beams on for a long time ($t \gg w_0^2/(2D)$), the following approximation holds:

$$\Delta T_{long}(0, 0, t) \approx \frac{AP_0}{2^{3/2}\pi^{1/2}w_0k} \tag{2.14}$$

Here, the peak temperature is proportional to the absorbed power per unit length, AP_0/w_0, and is constant with time. This is a steady state solution and can be used to compare the thermal properties of optical materials.

2.3.1 Melting

A laser damage threshold in the CW-regime can be defined by the power at which a material under laser irradiation reaches a critcal temperature and breakdown occurs. Following the short-pulse peak temperature in Equation 2.13, this can be written:

$$P_{th} = \Delta T_{cr} \frac{2^{3/2}\pi^{1/2} w_0 k}{A\sqrt{Dt}} \tag{2.15}$$

Here, ΔT_{cr} is some critical temperature. One candidate for critical temperature is the melting point. A temperature-induced phase change in an optical material is almost sure to cause catastrophic damage. In addition, melting and cracking during heating can cause extra absorption, leading to thermal runaway. Therefore, the material melting point is a reasonable place to start predicting a damage threshold for thermal damage. Table 2.4 shows a number of optical materials, their melting temperatures and the power per unit length required to get to the melting temperature, according to Equation 2.14. The values in the table assume a constant absorption coefficient of 1 ppm, and thermal conductivity was estimated from known values for approximately bulk materials.

Table 2.4: Calculated CW Laser Melting Thresholds

Material	Melting Temperature (K)[a]	Thermal Conductivity (W/(m K))[a]	Melting Power (kW/μm)[b]
SiO_2	1870	1.5	11.
HfO_2	3031	1.1	15.
TiO_2	2116	4.8	43.
Al_2O_3	2345	25.	250
Ta_2O_5	2145	33.	300

[a]bulk values assumed. Data from web database.

[b]Melting power calculated from Equation 2.15, with 1 ppm absorption.

It should be emphasized that the values in Table 2.4 are not laser damage thresholds. In practice, optical materials may break down at a power level much lower than that neeeded to reach the melting point [58]. There are a number of reasons why the laser damage threshold may be reduced from these values, including increased heating of non-infinite optical structures, the reduced thermal conductivity of thin films, thermal

expansion failures at below melting temperatures and non-linear absorption at high temperatures. Thermal laser damage has been cited as due to the pressure exuded by a laser-heated-and-expanded section of a material on the surrounding material [59, 60, 61, 58, 62]. The underlying reason for this is given by what happens to the material lattice when its temperature increases. The next section will go into depth on the physical nature of thermal expansion.

2.3.2 Thermal Expansion

Thermal expansion in solids is defined as a change in the space occupied by material with temperature [63]. A linear change with temperature is given in Equation 2.16.

$$\alpha = \frac{1}{3V}\left(\frac{\partial V}{\partial T}\right)_P \tag{2.16}$$

Here, the factor of 3 assumes linear expansion is 1/3 the magnitude ofa volume expansion in the 3 directions of space. Equivalently, thermal expansion can be thought of as a change in internal pressure or stress as a function of temperature [63]. This derivation of thermal expansion will show how the internal force of the material changes with expansion. The relationship between changes in volume and material pressure are given by the bulk modulus, $B = -1/V(\partial V/\partial P)_T$. Therefore, the thermal expansion in terms of pressure is:

$$\alpha = \frac{1}{3B}\left(\frac{\partial P}{\partial T}\right)_V \tag{2.17}$$

Pressure is a force per unit area. The force exerted by the molecular system is given by $F = -\partial U/\partial x$, where U is the internal energy of the system. As an example of internal energy, consider a two body system with an anharmonic Lennard-Jones potential:

$$\phi(x) = -\frac{2A}{x^6} + \frac{A}{x^{12}} \tag{2.18}$$

Where A is a constant chosen such that the energy minimum falls at $x = 1$. This can be expanded in x:

$$\phi(x) \approx -A_0 + A_2(x-1)^2 - A_3(x-1)^3 + A_4(x-1)^4 + O[(x-1)^5] \tag{2.19}$$

where A_i are the coefficients of the expansion. In practice, the interatomic potential may be something other than the Lennard-Jones potential given in Equation 2.18, but an expansion like that shown in Equation 2.19 may still be used to model anharmonicity. Figure 2.5 shows an example of the differences between the Lennard-Jones potential, the harmonic approximation and an order-4 anharmonic approximation.

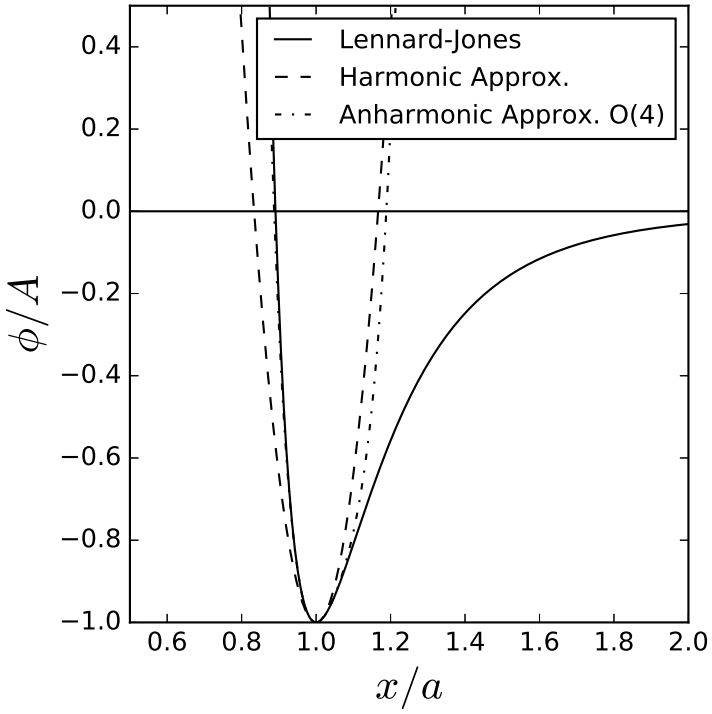

Figure 2.5: Interatomic potentials demonstrating differences between a realistic Lennard-Jones potential (solid line), a harmonic approximation (dashed line) and an order-4 anharmonic approximation (dot-dashed line). The additional terms in the anharmonic approximation result in a displacement-dependent material force.

The internal energy of the harmonic and anharmonic potentials we have considered can be given as:

$$U_{harm} = \frac{\partial^2 \phi(x)}{\partial x^2} u(t)^2 \tag{2.20}$$

$$U_{anh} = \frac{\partial^3 \phi(x)}{\partial x^3} u(t)^3 + O(4) \tag{2.21}$$

$$U_{tot} = U_{st} + U_{harm} + U_{anh} \tag{2.22}$$

Here U_{st} refers to the 0-order static potential and $u(t)$ represents a small displacement wave between the atoms. The force $-\partial U/\partial x$ is now dependent on the terms with $u(t)$ displacement. Given this formulation, the force is $\Delta U/u$. In the harmonic approximation, the force, $F = -Cu(t)$, is proportional to the displacement. In an anharmonic approximation, the force is $F = -Cu(t) + C_2 u(t)^2 + O(3)$. Assuming wave-like displacements (phonons), we can use a sinewave to approximate the displacement $u(t) = A\cos\omega t$. Thermodynamically, the force (or pressure) in the material will be a time average of the instantaneous force $\langle F \rangle = \int_0^\tau F(t)\, dt$. The time average of the harmonic term of the force, $F = -Cu(t)$, is zero, while the time-average of the anharmonic force is proportional to A^2. These relationships are given below.

$$\langle F \rangle_{harm} = -C \int_0^\tau A\cos\omega t\, dt = 0 \tag{2.23}$$

$$\langle F \rangle_{anh} = C_2 \int_0^\tau (A\cos\omega t)^2\, dt = \mathrm{c}_2 A^2 \int_0^\tau \left(\frac{1}{2} + \cos 2\omega t\right) dt = \frac{C_2 A^2}{2} \tag{2.24}$$

Therefore, only in the anharmonic approximation is the mean force a function of displacement amplitude. The energy of the two body oscillator is given by $E = CA^2/2$, where C is a stiffness term that comes from the curvature of the potential function $\phi(x)$. For a one-dimensional oscillator with two degrees of freedom, this energy will also correspond to $E = 2(kT/2) = kT$. Therefore, the mean force is a function of pressure $\langle F \rangle = C_2 E/C = (C_2/C)kT$. Thus, the thermal expansion is proportional to the harmonic over anharmonic spring constants: $\alpha \propto \partial\langle F \rangle/\partial T \propto C_2/C$. Therefore in the harmonic approximation, phonon frequency is independent of amplitude, whereas in the anharmonic approximation, phonon frequency is a function of amplitude.

In summary, vibrational states in solids are typically modeled as harmonic oscillators. This is because, near the minimum, the potential energy from one ion to another can be approximated by a 2nd-order polynomial. Harmonic oscillator states are the result of a quadratic potential. However, thermal expansion in solids is a result of the anharmonic parts of the interatomic potential. Only in the anharmonic description is

the average force a function of displacement. This displacement amplitude is a function of temperature. Therefore, anharmonic terms are needed to couple changes in temperature to changes in force, and thus expansion.

2.3.3 Thermal expansion and film stress

As was previously mentioned, optical materials may break down at temperatures much lower than the melting point. Local thermal expansion exerts a stress on an optical material that may exceed the breaking point. This is especially true for optical films. The relationship between film expansion and stress is given below [58, 62]:

$$\Delta\sigma_f = \Delta\alpha \frac{E_f}{3(1-2\nu_f)} \Delta T \tag{2.25}$$

Where $\Delta\sigma_f$ is the extra film stress due to thermal expansion, $\Delta\alpha$ is the coefficient of thermal expansion mismatch between film and substrate, E_f is the film Young's modulus and ν_f is the Poisson ratio for the film. Typically this equation will reduce the critical temperature from the melting point. For example, SiO_2 has a tensile strength on the order of 100 MPa. If $\Delta\alpha$ is on the order of 10^{-5}/K, the critical temperature is reduced from the melting point, 1870 K, to a thermal-expansion-induced-fracture point of 1148 K. Rearranging Equation , the fracture temperature can be given as:

$$\Delta T_F = \frac{3(1-2\nu_f)}{\Delta\alpha E_f}(S_F - \sigma_f) \tag{2.26}$$

where S_F is the tensile strength, or stress-to-fracture point, of the film and σ_f is the as-deposited film stress. Often, the tensile strength for compressive films is different than that of tensile films. In addition, thermal expansion can be positive or negative. The total expansion-induced-stress needed is dependent on the sign of the expansion and the sign of the as-deposited film stress. As an example of the expansion-induced critical-temperature-reduction, Table 2.5 shows some example parameters for optical coating materials deposited on SiO_2. Since all of the films considered have a CTE greater than that of SiO_2, the corresponding stress will have a negative sign as well. Assuming films have small as-deposited stress, a reasonable assumption can be made for compressive fractures occuring from 200-600 MPa. Numbers in the table refer to a film

stress increase of 300 MPa – assumed to cause fracture – as well as the same numbers and 1 ppm absorption as Table 2.4.

Table 2.5: Calculated CW Laser Film Fracture Thresholds

Material	Thermal Expansion Coefficient (10^{-6}/K)[a]	Fracture Temperature (W/(m K))[b]	Fracture Power (kW/μm)[c]
HfO_2	6	2700	8.7
TiO_2	9	540	3.8
Al_2O_3	8	590	24.
Ta_2O_5	4	1900	170

[a]bulk values assumed. Data from web database.

[b]Fracture temperature calculated from Equation 2.26 assuming fracture stress of 300 MPa

[c]Fracture power calculated from Equation 2.15, with 1 ppm absorption

The values in Table 2.5 show that films with a high thermal expansion coefficient (CTE) and high Young's modulus (TiO_2, Al_2O_3) tend to have worse fracture temperatures. In all cases, the power in W/m required to damage the films is significantly reduced from Table 2.4.

2.4 Conclusion

This chapter has presented the relevant theories of laser breakdown in dielectrics. After a summary of laser damage terminology and an overview of the optical materials considered, laser damage has been divided into regimes. Short pulse effects are primarily field-induced while longer pulse effects are due to absorbed power heating the material. The nonlinear absorption that occurs in high-field, short-pulse damage is due to multiphoton ionization and avalanche processes. The two processes are compared. There is some dispute about the validity and relative contributions of these mechanisms. Since our experiments were done with long-pulse laser systems, an emphasis has been placed on those damage effects. These effects differ in that material absorption is more or less linear during tests up until thermal runaway occurs. The time-dependent absorption that may occur appears to change primarily as a result of defect states and changes primarily right before catastrophic damage. Thermal expansion was presented

as they apply to laser damage and thermal measurement. With this background, the experiments of this work are presented next.

Chapter 3

CW laser damage of nanolaminate films

3.1 Introduction

Now that the relationship between material optical and thermal properties and laser damage has been established, a laser damage study is presented. This chapter describes a laser damage experiment done on an engineered optical coating[41]. Two types of coatings were compared. One type was designed to be amorphous and the other was grown as a polycrystalline film. The most desired optical coating materials for high power lasers are usually amorphous because, among other issues, it is thought that scattering from the grain boundaries of a polycrystalline coating will introduce stray light into the optical system and degrade the overall performance [64] and increase absorption [65]. Studies of laser-induced damage threshold (LIDT) as a function of material properties have been mostly performed with relatively short pulse laser radiation. Some of the early studies found that amorphous materials have higher laser damage resistance in the femtosecond regime due to increased resistance to avalanche breakdown [53, 66, 30, 67, 68]. The fundamental damage mechanisms in this regime are multiphoton absorption followed by free electron absorption and avalanche breakdown. These mechanisms are fairly accurate for describing damage in defect-free samples. However, it is well known that laser damage thresholds and mechanisms vary widely with pulse length [53, 69, 6]. Damage mechanisms in the continuous-wave (CW) regime are less

well understood. Studies have been performed with highly absorbing semiconductor samples [70, 71, 72] and coated dielectric optics [27, 73, 74, 28, 75]. These damage studies have described thermal distortion, phase change dynamics, and contamination but little is known about the role of material crystallinity. To our knowledge, the only other study of the laser damage threshold of nanolaminate (NL) films found that the nanolaminates had increased damage resistance over standard films for 1 ns pulses [76]. In that study, the authors attributed the increased damage resistance of the nanolaminate film to reduced optical scattering and, subsequently, reduced absorption, as in [64] and [65]. In this research presented below, we show that for long duration pulses and under CW illumination, polycrystalline materials have improved laser damage thresholds compared to amorphous nanolaminates, the opposite of the behavior for ultra-short pulses as found in the cited work above.

3.2 Thin Films

Thin Films. We performed laser damage experiments on two classes of coatings. The first was composed of uniform films of hafnia (HfO_2) and titania (TiO_2). The hafnia and titania films had thicknesses of 100 nm and 60 nm, respectively. The second class was nanolaminate films, composed of a primary film layered with a secondary film designed to mitigate crystal grain formation in the primary film [77]. For example, the nanolaminate hafnia film was grown by depositing 10 nm of hafnia, followed by 1 nm of alumina, and repeating this period 10 times for an approximately 100 nm total film thickness. Our alumina films are amorphous and serve to mitigate crystal growth in the hafnia films. A similar recipe was followed for the titania/alumina nanolaminate. We used an atomic layer deposition process for all films using a Cambridge NanoTech Savannah ALD system. The films were grown by pulsing 1 half-cycle of metalorganic precursor, followed by a nitrogen purge, followed by 1 half-cycle of water vapor, followed by a final nitrogen purge to complete the cycle. The hafnia metalorganic precursor was tetrakis(dimethylamido) hafnium (TDMAH), the titania precursor was titanium tetra(isopropoxy) (TTIP) and the alumina precursor was trimethylaluminum (TMA). Substrate temperature for all films was 250 °C. The crystallinity of the films was measured using both atomic force microscopy (AFM) and x-ray diffraction (XRD)

with films deposited on silicon substrates for testing purposes. The AFM measurements used a Brucker Dimension 3000 atomic force microscope in tapping mode and provided physical data on the surface roughness, which is often an indicator of the polycrystalline grain structure. The XRD data was collected on a Siemens D-500 Diffractometer and the crystallinity was quantified using Materials Data, Inc. JADE XRD analysis software and materials database. The data was collected for diffraction angles between 20 and 90 degrees and the results were compared against the JADE database of material XRD signatures. Crystallinity was quantified by a JADE algorithm which compares the area under the sharp crystal peaks in the data to the wider amorphous peaks. The nanolaminates had both smoother AFM profiles and drastically reduced crystal peaks in the XRD data than the uniform films, as shown in Fig. 3.1 and Fig. 3.2. Thus we found that the nanolaminates used in our study were indeed more amorphous than the films without the alumina spacer layers, as expected from prior research [77, 47].

3.3 Substrates

Substrates. The films were deposited on fused-silica substrates. The substrates had patterned regions as well as smooth, unpatterned regions. The patterned regions were designed as photonic crystal filters resonant at 1.55 μm [78]. The pattern design was as follows: the substrates were fused silica and had a hexagonal pattern of pits etched into the surface; the etch pits were 600 nm in diameter and 300 nm deep; the grating period was 1150 nm in the hexagonal crystal direction. We found that the uncoated substrates were very difficult to damage with our laser system at even the highest laser power levels. The patterned regions of the coated substrates appeared to have reduced damage thresholds but still had values near the limit of our ability to measure. On a pragmatic level, the patterned substrate made identifying damage sites easy.

3.4 Laser Damage System

Damage tests were performed by performing a row of 1-on-1 tests at constant irradiance while observing the samples for visible damage at 20x magnification. Our 1-on-1 tests consisted of 3 steps. First, we identified a test site free of visible defects. Second, we

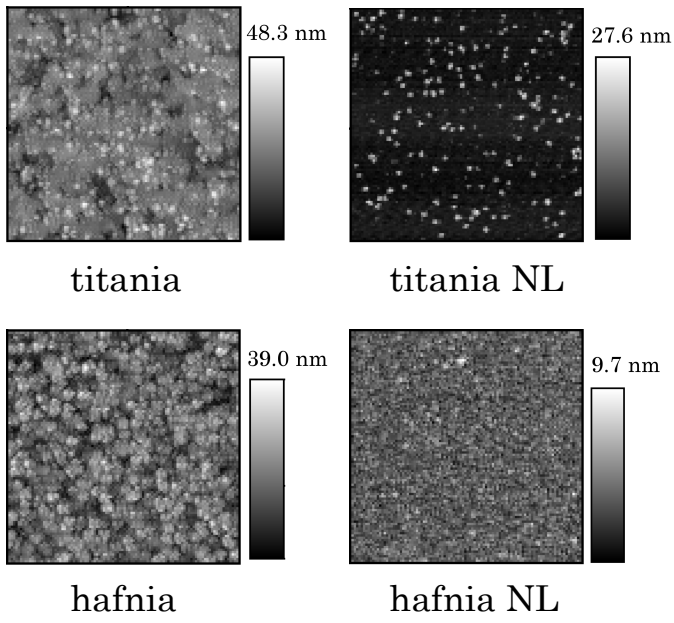

Figure 3.1: AFM measurement results for titania, titania/alumina nanolaminate (NL), hafnia, hafnia/alumina nanolaminate. Note change of scale bar between measurements.

irradiated the sample for 6s with either CW or pulsed radiation. The pulsed radiation was a 6 s pulse train of 60 ns Q-switched pulses at a pulse repetition frequency of 5 kHz. During this step we also measured the average beam power and beam profile. Finally, the sample was examined for damage before proceeding to the next test site. On average, 5 damage sites were tested per power level. We started with our maximum irradiance and then stepped to lower values until the damage threshold was reached. The damage thresholds were calculated as the average power levels at which damage occurred for approximately 50% of the tests. Our laser damage source was a multi-mode Nd:YAG Q-switched laser operating at a wavelength of 1064 nm. The beam was normal-incident. The spot size was nominally 200 μm. A small spot size was necessary to achieve high enough irradiance to cause damage. The laser power (average power for Q-switched pulses) was monitored using a Newport 818T thermopile detector. The beam waist was measured before focusing using a Cohu 4812 CCD camera and Spiricon analysis software. Lens equations were used to estimate the spot size after focusing.

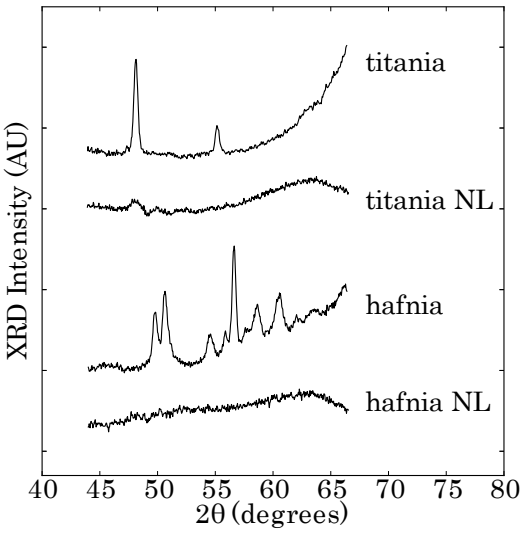

Figure 3.2: XRD measurement results for thin films (from top): uniform titania, titania/alumina nanolaminate, uniform hafnia, hafnia/alumina nanolaminate.

These calculations were verified at low power levels using the CCD camera. Accurate beam spot size measurement at the sample was difficult at high power levels and we relied on estimation. While damage threshold numbers carry significant uncertainty, the damage levels of the different film materials and morphologies were clearly distinct. The damage setup is shown in Fig. 3.3.

3.5 Laser Damage Threshold

We found that the uniform films clearly had higher damage thresholds than their nanolaminates for both hafnia and titania-based films, for both patterned and unpatterned substrates and for both 60 ns Q-switched pulsed irradiation and CW irradiation. Also, the hafnia films had higher damage thresholds than the titania films, in general. This agrees with other laser damage studies of the two materials [79]. This data is summarized in Tables 1 and 2.

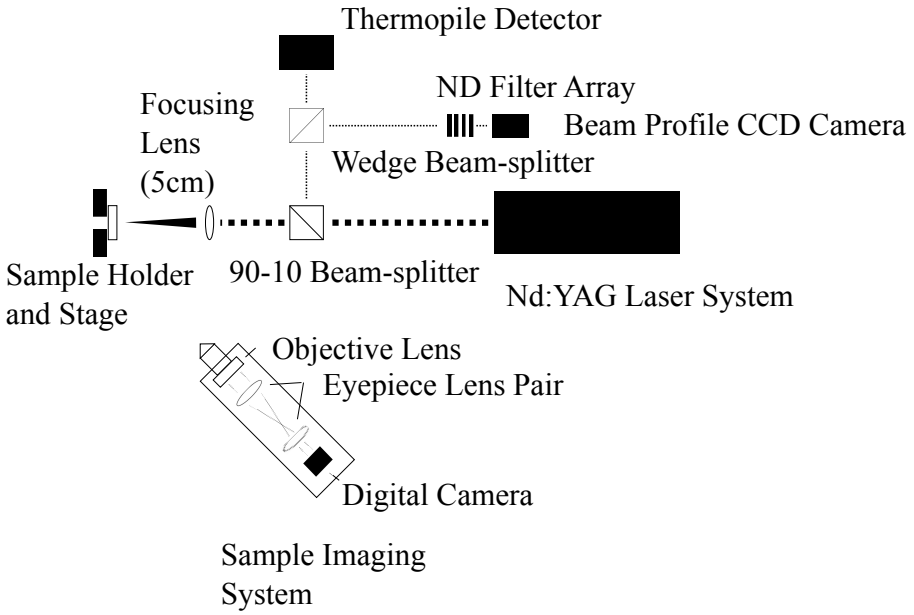

Figure 3.3: Laser damage experimental setup.

3.6 Laser Damage Phenomena

Almost all of the tests where the irradiation was significantly above threshold produced a plasma flash and audible acoustic shock wave in the air. This is indicative of material heating, ultrasonic wave generation and evaporation at the onset of damage [80, 81, 82]. The tests that produced audible shock waves did so within the first few milliseconds of the 6s laser irradiation, i.e. there were no tests which produced shock waves near the middle or end of the 6s irradiation. Uniform and nanolaminate films had different damage morphologies. Fig. 3.4 shows a 5x5 array of damage sites. Each horizontal row of sites was tested at the same power level. The power level was stepped from the high to low power levels from top to bottom in both images. The nanolaminate film had higher ratio of damaged sites to total test sites for each row of constant irradiance, except for the top row in which both films were damaged for all 5 tests. In addition, the damage spots of the nanolaminate film were larger in radius than the spots in the uniform film. Fig. 3.5 shows typical laser damage morphologies. In Fig. 3.5a, near threshold, laser damage spots were smaller than the beam width. In Fig. 3.5b, well

Table 3.1: Unpatterned Substrate LIDT[a]

Film	60 ns Pulsed LIDT (kW/cm^2)	CW LIDT (kW/cm^2)
Fused Silica (Substrate)	>190	>250
Hafnia	<190	230
Hafnia NL	<190	130
Titania	<60	80
Titania NL	<60	20

[a]Laser-induced Damage Threshold of the films deposited on a pristine, unpatterned region of the sample

Table 3.2: Patterned Substrate LIDT[a]

Film	60 ns Pulsed LIDT (kW/cm2)	CW LIDT (kW/cm2)
Patterned Fused Silica (Substrate)	>190	>250
Hafnia	110	160
Hafnia NL	70	100
Titania	10	30
Titania NL	1	5

[a]Laser-induced Damage Threshold of the films deposited on a patterned region of the sample

above threshold, spots were on the order of the beam width. The ring-like morphology may be due to shock wave generation or thermally-induced stress [79, 83].

3.7 Discussion

Our XRD and AFM data indicate that the nanolaminates have significantly reduced crystallinity. In addition, our laser damage studies show that the nanolaminates have reduced damage resistance to CW and 60 ns pulsed laser radiation. This is an interesting result because prior research on shorter pulse laser illumination has found the opposite dependence for nanolaminates using 1 ns 1064 nm pulses in [76], where nanolaminates had increased damage resistance. It is known that less crystalline hafnia and titania

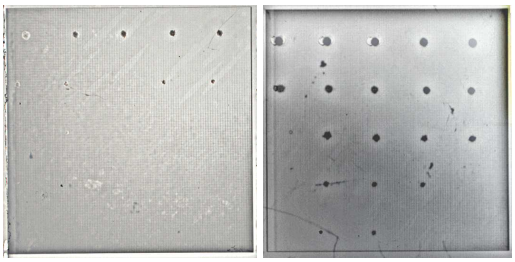

Figure 3.4: Optical microscope images of uniform titania-coated and nanolaminate titania-coated patterned-substrate damage test arrays . Each of the 5 horizontal rows comprising 5 test sites was tested with a constant irradiance.

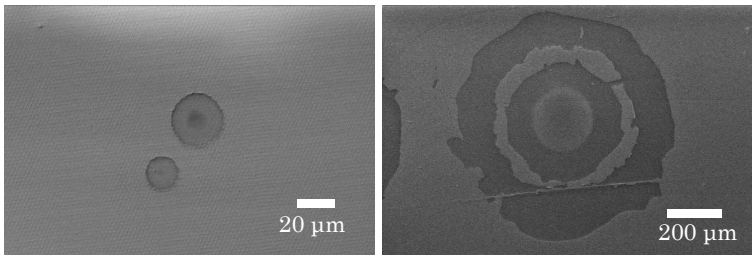

Figure 3.5: SEM images of hafnia nanolaminate laser damage test site morphologies after irradiation (a) near threshold and (b) well above threshold. Note change of scale.

thin films also have reduced thermal conductivity [84]. In our own prior work, we measured the crystallinity and thermal conductivity of hafnia nanolaminate and uniform ALD films [47]. We found that the uniform hafnia films had a thermal conductivity of 1.72 W/m K while the hafnia/alumina nanolaminate films had a thermal conductivity of 1.02 W/m K. Data on titania nanolaminate and uniform ALD films had a similar relationship. In addition to film thermal conductivity, film thermal expansion differences are known to affect laser damage resistance [85]. However, recent studies have implied that nanolaminates behave less like thin film multilayers and more like uniform amorphous materials with respect to stress and strain [86, 87]. Nevertheless, film stress

and thermal expansion should be measured in future work.

3.8 CW Laser Heating of Polycrystalline Films

Our experiment showed that, for films with varying crystallinity, there may be a tradeoff between film scattering properties and film thermal conductivity. This section comprises a theoretical treatment of the observed results. Typically, thermal conductivity is higher for more crystalline films. A difference of up to a factor of 2 has been observed for HfO_2 polycrystalline films vs. amorphous nanolaminate films on fused silica [47, 41]. Conversely, crystalline films my scatter light leading to increased absorption. This section will compare the contributions of scattering loss and thermal conductivity to laser heating. Since heating tends to drive damage, films which heat faster will tend to damage at lower thresholds. There is a crossover behavior where a film with high absorption and high conductivity may perform better at longer pulse lengths and worse at shorter pulse lengths. This crossover behavior is explored using Equation 2.12.

3.8.1 Scattering in polycrystalline films

As an example of the effect of crystal grains on absorption, consider the Rayleigh scattering from polycrystalline grains [88]. Rayleigh scattering holds when the scattering particle radius is much smaller than the wavelength. If we assume a wavelength of 1 μm, then particles smaller than 10 nm can be approximated by Rayleigh-Gans-Debeye scattering [89]:

$$\sigma_R = \frac{8\pi^3 r^4}{\lambda^2}\left(\frac{\Delta n}{n}\right) \tag{3.1}$$

Here, σ_R is the Rayleigh scattering cross-section, r is the grain size, λ is the wavelength of light and $\Delta n/n$ is the percent change in refractive index. The scattering cross-section is multiplied by the scatterer density to calculate a loss coefficient. If we assume the scatterer density is given by a closest-packed sphere density, it is $N = (8\pi r^3/3)^{-1}$. Multiplying this by the scattering cross-section results in a scattering loss coefficient:

$$\alpha_R = 3\frac{\pi^2 r}{\lambda^2}(\Delta n)^2 \tag{3.2}$$

This scattering loss is multiplied by a film thickness to determine total loss to scattering. For a 100 nm film, a 0.001% change in scatterer refractive index, particle size of 15 nm and wavelength of 1 μm, total loss due to scattering may be 0.04 ppm. This loss may be available to the film for re-absorption, thus contributing to a lowered damage threshold. In practice, increased scattering may have an even stronger effect due to nonlinear absorption or increased coverage of sparse absorption centers. Thus a film may simultaneously have increased thermal conductivity as well as increased absorption.

3.8.2 Pulse-length dependence of long-pulse damage

For certain films, there is a crossover behavior from intensity-dominated during short-pulse irradiation to a thermally-dominated long-pulse regime [76, 41]. In one regime, film absorption properties are most important and amorphous films with reduced scattering may be desirable. In the other regime, film thermal conductivity may play the dominant role, allowing the film to dissipate the heat faster. Equations 2.9 and 2.12 can be evaluated to describe the rise and fall of temperature due to two pulses of the same intensity, but different pulse times. For two films with identical density and heat capacity, but with the second film having an absorption coefficient 1.8 times that of the first film as well as a thermal conductivity of 2 times that of the first film, the short pulse vs. long pulse behavior is elucidated in Figure 3.6.

Here we clearly see that two otherwise similar films may have different crystalline structures, which affects their laser damage performance in short-pulse vs. long-pulse regimes. A film designer may prefer a film with less absorption for short pulses, or may prefer a film with greater thermal conductivity for longer pulses. The transition point for the two film types can be found if the film absorption and thermal conductivities are known. For the purposes of a mathematical comparison, the time at which the two films have the same absorbed power is given, using Equation 2.12, below:

$$\frac{A_1 P}{2^{3/2}\pi^{1/2} w_0 k_1} \arctan\left(\frac{\sqrt{2D_1 t}}{w_0^2}\right) = \frac{A_2 P}{2^{3/2}\pi^{1/2} w_0 k_2} \arctan\left(\frac{\sqrt{2D_2 t}}{w_0^2}\right) \tag{3.3}$$

Let $k_2/k_1 = \xi$, $A_2/A_1 = \zeta$, and $\tau = \sqrt{2D_1 t}/w_0$. Given $D_2/D_1 = \xi$, Equation 3.3 can be simplified as follows:

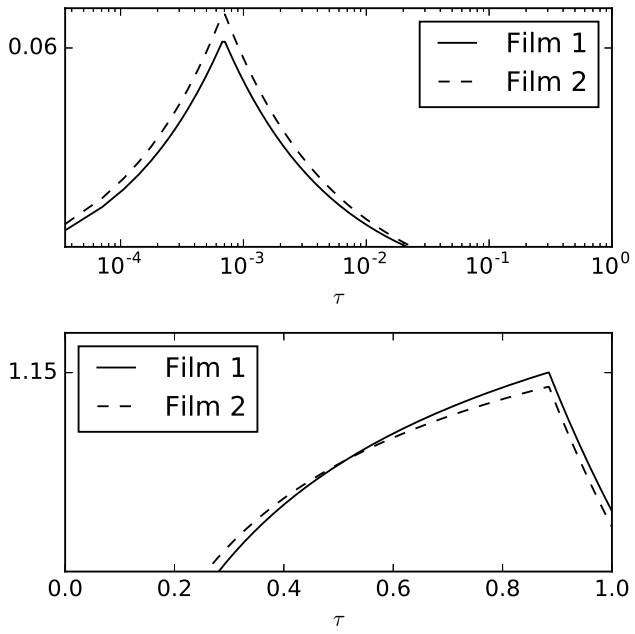

Figure 3.6: Short-pulse heating (top) vs. long-pulse heating (bottom) for 2 films. Note that Film 2 has increased temperature (y-axis) during short pulse heating, but has lower temperature during long-pulse heating. Film 2 has absorption equal to 1.8 times that of Film 1. Film 2 has thermal conductivity equal to 2 times that of Film 1. Y-axis is in arbitrary units, but is consistent between the two graphs. X-axis is in units of thermal diffusion time $\tau = \sqrt{2Dt}/w_0^2$.

$$\arctan\sqrt{\tau} = \frac{\zeta}{\xi}\arctan\sqrt{\xi\tau} \tag{3.4}$$

Rearranging again recovers an equation that can be plotted for a series of ratios.

$$\tau + 1 = \sec^2\left(\frac{\zeta}{\xi}\arctan\sqrt{\xi\tau}\right) \tag{3.5}$$

A few plots with different absorption ratios is given in Figure 3.7. It should be noted that there are many combinations of ξ and ζ for which there is no transition time, i.e. one film will always reach a higher temperature. However, for similar films, this discussion may inform a selection of film properties for a given laser pulse time.

It should also be noted that this discussion assumes only linear absorption. We have assumed both irradiences will be equal, but in practice shorter pulses are often at a higher irradience for shorter times and therefore are more likely to incur non-linear effects. This is a difficulty in comparing short pulse and CW systems in general.

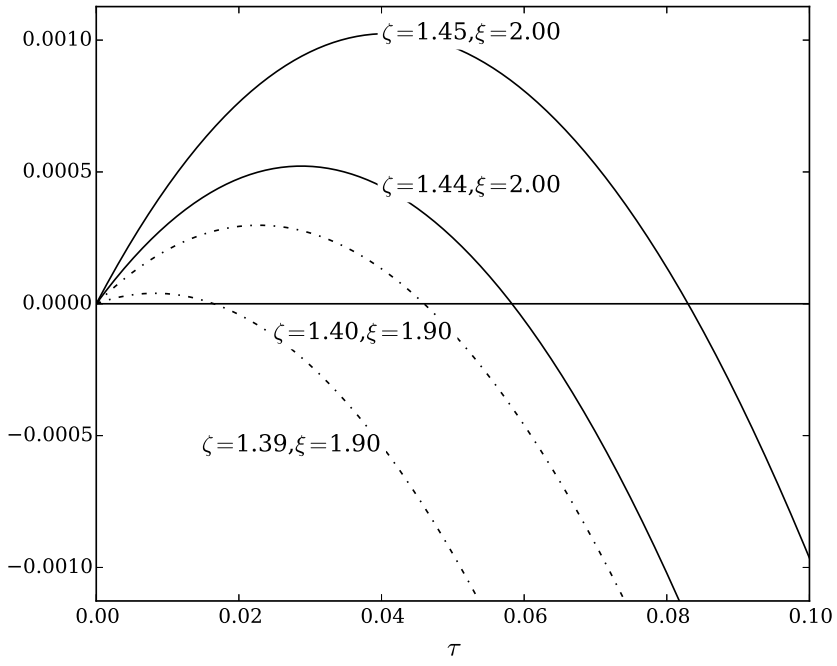

Figure 3.7: Laser heating transition time comparison for two films for a few example cases. The vertical axis is the unitless output of Equation 3.5. The films are identical except for thermal conductivity and absorption, where $\xi = k_2/k_1$ and $\zeta = A_2/A_1$. Time is in units of thermal diffusion time for a given beam waist: $\tau = \sqrt{2D_1 t}/w_0$. The figure shows that as films become more dissimilar in thermal conductivity and absorption, the transition time increases.

3.9 Laser Damage Morphology

In addition to post-hoc craters, a visible plasma plume and an audible acoustic shock wave often accompanied tests producing damage. The plasma plume may provide valuable information about the chemistry of the vaporized material. The acoustic shock wave was recorded with a single sonic microphone element. Tests with pulsed irradiance produced acoustic wave spectra peaked around the Q-switch frequency at 5 kHz.

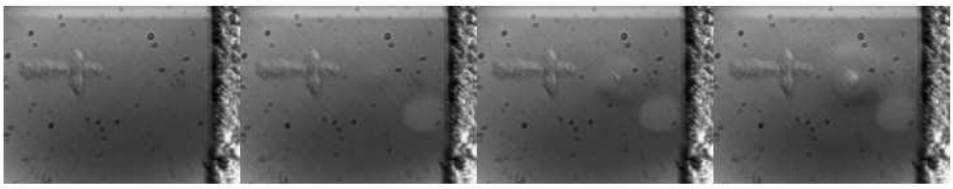

Figure 3.8: Four consecutive frames from a high-speed schlieren imaging system. The frame rate was 10,000 fps. The first frame was taken immediately following a laser pulse was absorbed by the sample. Thermo-mechanical waves are visible as the frames progress.

Later measurements showed surface waves that were visible with an in situ Schlieren high-speed imaging system. This system used a high-speed camera with a fast shutter and a frame rate of a few multiples of the laser pulse frequency. This allowed us to capture different phases of fast periodic phenomena as well as slower surface changes. Figure 3.8 shows measurements made with the system. In the figure, the cross-like feature was from a previous damage test and the bright oval to the lower right of focal point was due to glare in the imaging system. A wave-like feature appears to develop over the 4 frames shown. These measurements indicated the presence of thermo-elastic waves in the samples, which are likely responsible for the surface morphologies detailed in the next section.

As seen in Figure 3.5 and 3.9, some laser damage features had a unique bull's-eye pattern. These patterns appeared in approximately 10% of damage features. These features were remarkably Bessel-like as shown in 3.10.

Figure 3.10 shows ring-like features consisting of a central crater of substrate damage as well as film delamination surrounded by a ring of still-laminated film, followed by

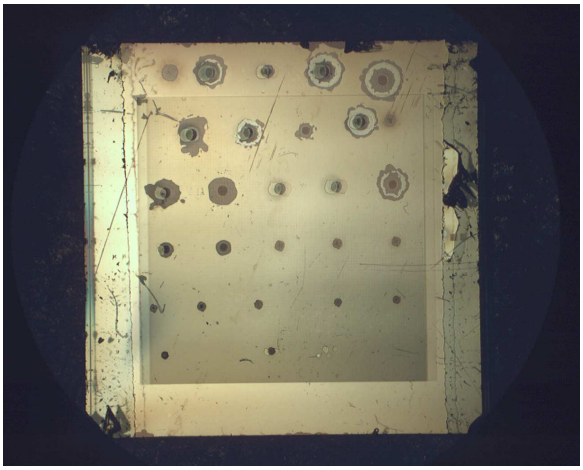

Figure 3.9: Laser damage test array showing a few bull's-eye feautures and other complex morphologies produced during laser damage testing.

another ring of delaminated film, before reaching the final extent of the visibly damaged region. These rings matched remarkably well with the first zeros of the zeroth-order Bessel function of the first kind with 96% accuracy by the following method: R1 and R2 are defined as the distance from the center of the feature to the center of the undelaminated film ring and to the edge of the total crater, respectively. R1 was matched to the first trough of a J_0 Bessel representing a temperature distribution. R2 was matched to the first peak of the J_0 Bessel (aside from the peak at the origin). x_1 and x_2 are defined as the locations of the first J_0 Bessel trough and first J_0 Bessel peak, respectively. The Bessel distribution shown in Figure 3.10 is flipped vertically to show matching with morphology features. A preliminary analysis was performed using standard heat transfer solutions. It was assumed that heating caused the film delamination and thus the Bulls-eye delamination pattern is indicative of an underlying Bessel temperature distribution. The derivation in Carslaw and Jaeger[90] is repeated below:

$$\frac{\partial T}{\partial t} = D\nabla^2 T \tag{3.6}$$

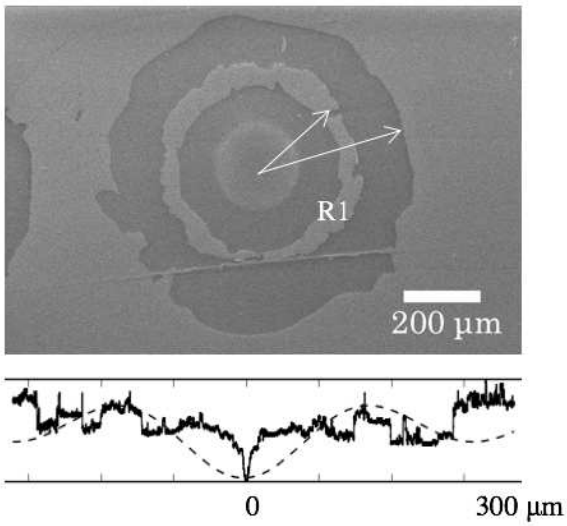

Figure 3.10: SEM image of ring-like damage features on an HUF-coated, patterned optical sample. Below is a profilometer scan across the center of the damage feature in the above image. A Bessel fit is superimposed in a dashed line. The bessel fit the damage features with 96% accuracy.

$$T(r=a)=0,\ \frac{\partial T}{\partial z}=0,\ \left.\frac{\partial T}{\partial r}\right|_{r=0}<\infty \tag{3.7}$$

$$T(r,t)=\sum_{n} a_n \mathrm{J}_0(\kappa_n r)e^{-D\kappa_n^2 t} \tag{3.8}$$

Here D is the thermal diffusivity and κ is a Bessel parameter. Also, r, z, t and T are spatial and temporal variables and temperature distribution, respectively. In this treatment, Bessel zeros, specifically the parameter κ, are functions of substrate and film thermal properties. Assuming thermal conductivity is the predominant difference between samples, Bessel-zero ratios are related to thermal conductivity ratios by inverse root:

$$\frac{x_1}{x_2}=\sqrt{\frac{\tau_1 D_1}{\tau_2 D_2}}\approx\sqrt{\frac{\tau_1}{\tau_2}}\approx\sqrt{\frac{k_2}{k_1}} \tag{3.9}$$

Here, x_n is the radius of the first ring of the Bessel bull's-eye. Also, D is thermal diffusivity and τ is the thermal time constant, related by $L^2=4D\tau$, where L is the film thickness (assuming uniform temperature in the film depth). The ratio of zeros for

two known film types was compared to known thermal conductivities for these films. Measurements showed that the hafnia nanolaminate films had thermal conductivity of 1.02 W/m-K, which is lower thermal conductivity than hafnia uniform films (1.72 W/m-K)[6]. Note that the substrate thermal conductivity is known to be approximately 1.4 W/m-K, which is between that of the films. The ratio is given below:

$$\sqrt{\frac{k_{NL}}{k_U}} = \sqrt{\frac{1.02}{1.72}} = 0.77 \tag{3.10}$$

Then, the bulls-eye ring radii were measured for hafnia-uniform and hafnia-nanolaminate films. It was found that the bulls-eye radius was larger for the nanolaminate bulls-eye than the uniform film bulls-eye.

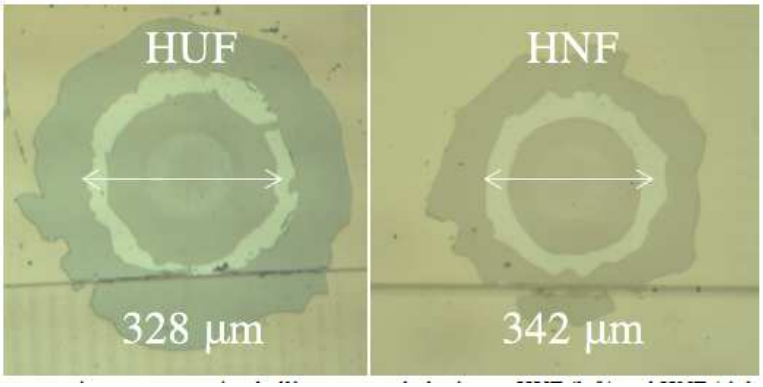

Figure 3.11: Optical microscope images comparing bulls-eye morphologies on a hafnia uniform film (left) and a hafnia nanolaminate film (right). In the features measured, the hafnia uniform film had a smaller bulls eye ring. The ratio is 0.96, which differs from the 0.77 estimate, given by thermal conductivity measurement.

As shown in Figure 3.11, the ratio of the measured bulls-eye diameters was different than the ratio given by the thermal conductivity relation in Equation 3.10:

$$\frac{d_U}{d_{NL}} = 0.96 \tag{3.11}$$

This means that bulls-eye morphology is not a function of film thermal conductivity alone. Other possible causes for this morphology are under investigation. Simple optical diffraction is unlikely. The distribution does not match the Airy disk and the high

number of laser modes present make ring-like mode interference unlikely. Further work will aim to accurately reproduce these features in an effort to more clearly understand how they are formed.

3.10 Conclusion

These results may indicate that in the CW regime, pure heat transfer effects begin to dominate high-field damage mechanisms and the impact of light scattering may be relatively less. Hafnia/alumina and titinia/alumina nanolaminate films, designed to mitigate film crystal growth, have significantly reduced laser damage resistance to CW radiation compared to their polycrystalline single material films. We speculate that the more-crystalline uniform films were better able to dissipate the absorbed energy because of their higher thermal conductivity. Our experimental measurements and theoretical model backs up this assumption. In addition, we observed anomalous damage features that we were unable to explain with initial theoretical treatments. We proceed to explore the laser heating with high-speed experimental imaging in the chapters to follow.

Chapter 4

Thermal deformation waves in transparent media

4.1 Introduction

While a quantitative study of laser damage has been presented, further details into the laser damage dynamical process are still hidden. We simply analyzed the samples before and after laser irradiation events. In order to probe further into the laser damage process, a high-speed measurement technique is needed. Work on such a system was performed and thermal measurements were made. This chapter consists of an explanation of the experimental setup, the theoretical background of the thermo-optic effect and heating models and the results of the measurements and data analysis. The problem was tackled by separating the laser damage dynamics into different temporal regimes. Photon absorption timescales may be quite fast, on the order of picoseconds. Electronic plasma development due to thermal carrier generation or multiphoton absorption may be on the order of nanoseconds. Mechanical waves due to photon pressure or thermal-mechanical deformation would likely occur on the order of microseconds. Thermal effects were likely the slowest process, as thermal diffusion in dielectric materials occurs on the order of hundreds of microseconds. We chose the slowest proccess as a target for our high-speed analysis system [91]. High-energy and high-power laser beams remain critically important for diverse tasks, from precise machining of materials [92] to measurement of small physical quantities [93] to generation of explosive plasmas [94].

High-energy ultra-short pulsed laser systems can achieve extremely high fields and have seen increased use in scientific and industrial applications requiring precise amounts of intense radiation. However, long-pulse and continuous-wave (CW) systems are often vital for specific applications requiring steady radiation to maintain high temperatures at a surface. The design of high-power long-pulse and CW laser systems has unique challenges. The damage process during ultra-short pulse irradiation has been well explored theoretically and experimentally to follow from field-induced carrier generation in pristine samples [6, 53, 95, 50]. Fast pump-probe imaging studies have shown excellent agreement with carrier-induced breakdown theory [96, 97, 25]. On the other hand, CW damage often involves thermal effects from the longer irradiation time that are unrelated to ultra-short pulse field effects. Samples that perform well during short-pulse irradiation may actually perform poorly during CW irradiation. For example, polycrystalline films have higher scattering than amorphous films, resulting in diminished short-pulse performance [76], yet they also have higher thermal conductivity, which improves their CW performance [47, 41]. CW irradiated samples have been known to break down during irradiation well after the substrate has reached steady state in field and temperature. Furthermore, the damage morphology and topography of a CW breakdown event can be more complex, involving larger volumes of material with more computationally-intensive modeling than short-pulse damage. Some damage features apparently are the result a combination of thermal and mechanical effects, which warrant further study [98].

In exploring these issues, it is desirable to have a monitoring system, which is able to observe temperature and mechanical variations at timescales faster than the thermal diffusion time. Furthermore, the temperature measured could potentially be a part of a single irreversible thermal process (i.e. laser damage). We desired an experimental setup with the ability to capture individual irreversible events. Therefore, chopped or stroboscopic methods for measuring periodic events could not be used. Traditional thermal cameras have frame rates that are too slow and therefore this technique was also unavailable. In glass substrates, the thermal diffusion time is on the order of 1 millisecond ($\tau = L^2/D$, where L = 25 μm and D = 5×10^{-7} m^2/s). We have developed a 2-dimensional monitoring system capable of capturing phase images of the sample surface at a rate of 11,800 frames-per-second (fps). These phase images correlate well

with thermal phenomena via substrate thermal expansion and temperature-dependent refractive index effects.

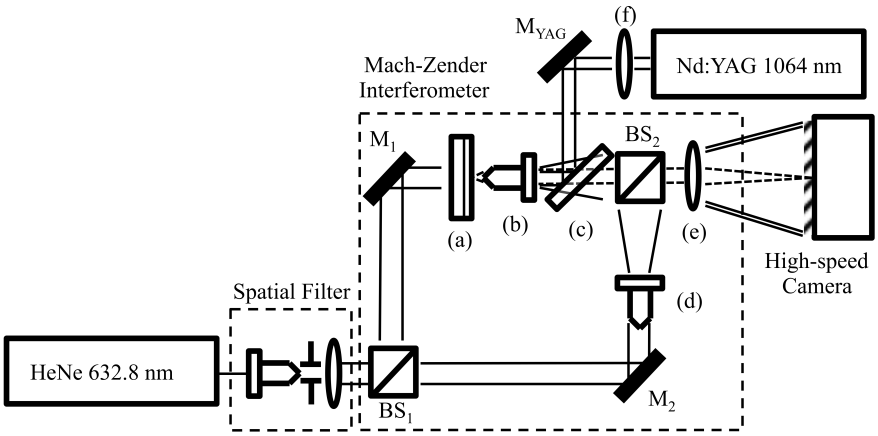

Figure 4.1: High-speed phase measurement system. Our system utilized a HeNe laser, a Mach-Zender interferometer and a high-speed camera. The Mach-Zender interferometer was composed of mirrors M1 and M2 and non-polarizing beam-splitters BS1 and BS2. The temperature of (a) a yttria-coated glass slide was imaged with (b) an objective asphere lens and (e) camera lens. The image was compared with a reference beam traversing (d) an identical lens. The angle between beams was such that the temperature distribution was due to energy absorbed by a high-power Q-switched Nd:YAG laser coupled-in via (c) a dichroic mirror that reflected 1064 nm light and transmitted 632.8 nm light. Since the two lasers shared an objective lens, (f) a dispersion-compensating lens was necessary. The interferograms captured with the high-speed camera were transferred to a computer for conversion.

4.2 Experimental setup

Our experiment studied the temporal decay of the thermal wave created by laser energy absorbed by our yttria-coated microscope slide sample. The microscope slide was a Gold Seal 3010 soda lime silica glass slide. A distributor, Ted Pella, Inc., listed glass slide composition as follows: 72.2% silicon dioxide, 14.3% sodium oxide, 6.4% calcium oxide, 4.3% magnesium oxide, 1.2% aluminum oxide, 1.2% potassium oxide, 0.03% sulfur trioxide, 0.03% iron oxide. The yttria coating was deposited by thermal evaporation

and was 300 nm thick. The total sample absorption was 0.1% as measured by our photothermal common-path interferometry system. We did not notice significant difference in uncoated sample absorption vs. coated sample absorption. To measure the temporal decay of a thermal wave, a fast method of measuring temperature was needed. Phase measurement methods are often a convenient way of measuring physical quantities with traditional optical instruments. In particular, a Hilbert phase imaging technique suitable for transmission methods was developed for relatively high speed imaging systems [99]. We extended this system for use with an even higher frame rate camera with a suitably powerful probe beam, as shown in Figure 1. This required redesign of the magnification loop to meet our imaging needs as well as a different compensation scheme in the reference arm. We opted for an identical lens in the reference arm to simplify the setup. A common camera lens refocused the interfering light from both arms onto the camera. We added ND filters in the reference arm to compensate for the loss in the sample arm. We also added the ability to couple in an on-axis pump beam. Our system utilized an adapted Mach-Zender interferometer (MZI), operating at a wavelength of 632.8 nm, a high-speed camera capable of up to 20,000 fps and appropriate thermal models for substrate dynamics. In addition to commercial off-the-shelf optics, we utilized a polarized 15 mW JDSU HeNe laser, which was spatially filtered to be single mode, and an IDT NX4-S3 high-speed camera. We captured videos of our sample surface irradiated by Q-switched pulses from a multi-mode Nd:YAG laser operating at 1064 nm with a pulse width of 100 ns, a pulse energy of 10 mJ and a repetition rate of 2 kHz. Our Nd:YAG system was manufactured by U.S. Laser Corp. as model number 405-Q. We coupled the high-power pump beam via dichroic mirror, which transmitted the probe beam. This coaxial imaging system allowed the use of a commercial high numeric aperture objective lens for both pump and probe beams. The focused spot size of the Nd:YAG beam was approximately 10 microns. There was difficulty verifying this because the focused beam was too intense for use with a camera and it damaged our knife-edge methods. The beam width and M2 were measured before focusing by a laser-beam analyzer and the focused spot was calculated. Our calculated beam waist was later verified by experimental data from the phase measurements. The sample was back-illuminated with the HeNe beam, which had a beam width of 3 mm. The image magnification system allowed a sample view area of 100 microns square. This sample

area was magnified to fill an area on the 1 focal plane array of the high-speed camera. A smaller-than-maximum area was used to increase the camera frame rate. The small spot sizes and Rayleigh ranges of the pump and probe beams helped guarantee that the measurement was highly localized to the sample surface. Table 1 summarizes the experimental parameters used in this study.

Table 4.1: Experimental parameters

Symbol	Parameter	Value	Units
$\lambda_{Nd:YAG}$	Nd:YAG wavelength	1064	nm
t_{pulse}	Nd:YAG pulse width	100	ns
f_{pulse}	Nd:YAG pulse repetition rate	2	kHz
E	Nd:YAG pulse energy	10	mJ
w_0	Nd:YAG beam width	10	μm
M^2	Nd:YAG multimode parameter	10	–
λ_{HeNe}	HeNe wavelength	632.8	nm
w_{HeNe}	HeNe beam waist (in MZI)	3	mm
τ_{cam}	Camera shutter speed	1	μs
f_{cam}	Camera frame rate	11800	fps

The interferograms produced by the phase measurements were stored as raw images and then later converted to temperature by computer post-processing. An example of this process for a frame captured <84 s after an Nd:YAG pulse is shown in Figure 4.2. The interferograms were first converted to phase images by way of an algorithm described in [99]. Our phase-unwrapping technique utilized an open-source algorithm and code developed in [100]. The phase was then converted to optical path length. Our conversion is detailed in the next section. We assumed the phenomenon was primarily temperature dependent, so this optical path length was considered to be a function of temperature. Typically, temperature-to-phase conversions are a sum of thermal expansion terms and temperature-dependent refractive index terms. There is some uncertainty with these conversions as they rely on a priori knowledge of material constants. However, assuming the temperature is a close function of phase, the temporal decay of the temperature profile can be found from the phase data. Thermal diffusivity can be

extracted from the temporal data without knowledge of absolute temperature. Figure 4.2(g) shows the initial spatial pulse shape of the observed wave. This decayed with time and spread out spatially (shown in Figure 4.6), leading us to assume we were observing thermal phenomena.

4.3 Theoretical background

The surface deformations in this work were assumed to be due to sample heating. The laser-induced temperature distribution can be observed via its effect on the optical properties of the sample. Temperature affects the optical path of the sample in the interferometer through both thermal expansion as well as the change in refractive index with temperature (thermo-optic effect or dn/dT). The thermo-optic effect will be discussed briefly next.

4.3.1 Thermo-optic Effect

In addition to damage, changes in optical properties of materials can change device performance. This may influence energy transfer and lead to damage, but it may also simply render a system useless due to increased scattering or diffraction. As previously discussed in Section 2.3.2, thermal expansion is one such effect. It influences the mechanical properties of materials, but it also may cause an optical system to perform less optimally. Another, often stronger, effect is the thermo-optical property, denoted $\partial n/\partial T$, in 1/K. While CTEs may be on the order of 5×10^{-6} (see Table 2.5), thermo-optic coefficients are often greater, on the order of 10^{-5} for SiO_2 and greater for semiconductors and polymers. Thus the thermo-optical property plays a major role in laser-material heating. In addition, it has served as a valuable means of measuring absorbed energy via photo-thermal common-path interferometry (PCI), thermal lensing and holographic thermal imaging.

The physical origin of the thermo-optic effect is in the temperature-dependence of the material polarizability as well as the temperature-dependence of material density, i.e. thermal expansion. Refractive index is typically a function of the more basic material polarizability, P, as well as density ρ. An example of the relationship between refractive index and density is given by the Lorentz-Lorenz equation, appropriate for a collection

of non-interacting dipoles in a medium [101]:

$$\frac{n^2-1}{n^2+2} = \frac{N_p}{3\epsilon_0}p \tag{4.1}$$

Where n is the refractive index, p is the mean polarizability (often denoted α, but it has been termed p to avoid confusion with the coefficient of thermal expansion) and N_p is the number of atoms per unit volume. To find the thermo-optic coefficient, this expression can be differentiated with respect to temperature [102]:

$$\frac{\partial n}{\partial T} = \frac{(n^2-1)(n^2+2)}{6n}(\gamma - \alpha) \tag{4.2}$$

Here, γ is the change in mean polarizability with temperature and α is the change in density with temperature, equivalent to the coefficient of thermal expansion. Therefore, the thermo-optic coefficient, while a separate effect, still includes thermal expansion as it effects the dielectric constant of the material. The temperature dependences are as follows:

$$\gamma = \frac{1}{p}\frac{\partial p}{\partial T} \tag{4.3}$$

$$\alpha = \frac{1}{\rho}\frac{\partial \rho}{\partial T} = -\frac{1}{V}\frac{\partial V}{\partial T} \tag{4.4}$$

The origin of γ is in the changes in material response to electromagnetic waves with temperature.

An alternative approach of investigating the thermo-optic effect is by looking at changes in material resonance with temperature. In the near-IR and visible spectra, the contribution of electronic valence-conduction band transitions dominates the electromagnetic response. The refractive index can be expressed as a function of photon energy according to a Forouhi-Bloomer equation of the form [103]:

$$n(\hbar\omega) = n_\infty + \frac{B_0\hbar\omega + C_0}{(\hbar\omega)^2 - 2\Delta E\hbar\omega + \Delta E^2 + (\hbar/\tau)^2} \tag{4.5}$$

Here, n_∞, B_0, C_0, ΔE and τ are material parameters to be defined shortly. This equation is derived from a semi-classical treatment of a lightwave interacting with the electronic states of a medium. Absorption transitions can be most easily described with

this treatment. They are converted to the dielectric response via the Kramers-Kroenig relations. The parameters in Equation 4.5 have a physical interpretation as follows [104]:

$$B_0 = \frac{A}{\hbar/\tau}\left(-\frac{4\Delta E^2}{2} + 2E_g\Delta E - E_g^2 + \Delta E^2 + (\hbar/\tau)^2\right) \tag{4.6}$$

$$C_0 = \frac{A}{\hbar/\tau}\left((E_g^2 + \Delta E^2 + (\hbar/\tau)^2)\Delta E - 2E_g(\Delta E^2 + (\hbar/\tau)^2\right) \tag{4.7}$$

Here E_g is the material bandgap, ΔE is the allowed energy of the transition and τ is the transition lifetime. The parameter A is the dipole matrix element of the transition. It is given by:

$$A \propto |\langle 2|x|1\rangle|^2\hbar/\tau \tag{4.8}$$

Here, $|1\rangle$ and $|2\rangle$ describe two states of the electronic system. This formulation shows the fundamental dependence of refractive index on the material electronic parameters E_g and the transition lifetime τ. An example of SiO_2 in the near-UV is shown in Figure 4.4.

Both the bandgap and transition lifetime are temperature dependent. An example of this is in the electron-phonon coupling model. The phonon contribution to the bandgap and transition lifetime can be approximated using the Einstein model [104].

$$E_g(T) = E_g(0) - \frac{2a}{\exp\left(\Theta_E/T\right) - 1} \tag{4.9}$$

$$\tau(T) = \tau(0) - \frac{2b}{\exp\left(\Theta_E/T\right) - 1} \tag{4.10}$$

Parameter Θ_E is an average temperature of phonons interacting with the electronic system. Parameters a and b are strengths of average electron-phonon coupling corresponding to bandgap and lifetime, respectively. From a fit to experimental data in [104], parameters for TiO_2 are as follows: a Θ_E temperature of 390 K can be used, and parameters a and b may be 0.109 and 0.091, respectively. The thermo-optic coefficient for TiO_2 at 300 K therefore is calculated as approximately $dn/dT = 9 \times 10^{-5}$ 1/K, for photon energies below the bandgap. Figure 4.5 shows the wavelength dependence of the

thermo-optic coefficient for TiO_2 at two different temperatures. Note that for photon energies below the bandgap, dn/dT is positive, whereas for photon energies above the bandgap dn/dT is negative.

Common optical materials have thermo-optic coefficients between 10^{-5} and 10^{-4} for bulk materials. However, for thin films this number may be reduced or negative, depending on how film thickness affects the contributions due to polarizability and expansion in Equation 4.2. Common bulk values are shown in Table 4.2.

Table 4.2: Thermo-optic coefficients for Bulk Optical Materials

Material	Thermo-optic Coefficient (10^{-6}/K)[a]
SiO_2	10
HfO_2	5.8
TiO_2	3.5
Al_2O_3	13
Ta_2O_5	12

[a]bulk values assumed. Data from web database.

In summary, the thermo-optic coefficient of dielectric solids is a function of thermal expansion as well as the temperature-induced changes in polarizability. We have seen that the refractive index is a function of material bandgap and electronic relaxation time. Calculation of dn/dT based on bandgap, relaxation time and thermal expansion results in values close to those found from experiments.

4.3.2 Heating Model

Another effect that could produce surface deformation is photon pressure due to the high-power laser beam pushing on the sample surface. However, photon pressure was calculated to be appreciable only at microsecond timescales at high energies, given the study in [105]. Additionally, many mechanical phenomena involve a restoring force, which produces an inflection point in mechanical waves that should not be present in thermal waves and was not present in our data. To analyze experimental results, a theoretical model for the temperature distribution of a heated substrate was needed. Our temporal resolution was on the order of 100 microseconds, and we observed no

anomalous behavior near the peaks. Therefore, we assumed a temperature-dependent explanation for the observed phenomena. The temperature profile for short pulse laser heating has been calculated to have a product-solution form in cylindrical coordinates [56, 37], shown in Equation 4.11, below.

$$\Delta T = \frac{AE}{2\pi^{3/2}\rho c\sqrt{Dt}\left(w_0^2 + 2Dt\right)} \exp\left[-\frac{r^2}{2\left(w_0^2 + 2Dt\right)}\right] \exp\left[-\frac{z^2}{4Dt}\right] \tag{4.11}$$

Here, AE is the absorbed energy, w_0 is the beam waist (see Table 4.1), ρc is the heat capacity, D is the thermal diffusivity (see Table 4.3) and r, z, t are radial, depth and temporal coordinates, respectively. Here, short pulse means the laser pulse is short compared to the thermal diffusion time. We observed diffusion times on the order of milliseconds while the laser pulse length was under 100 ns, so our product solution temperature profile was a safe assumption.

A useful quantity for optical path measurements is the integral of the temperature distribution into the sample, along the z-direction. This integrated quantity, at the center of the distribution ($r = 0$), is shown in Equation 4.12.

$$\int_{path} \Delta T \, dz = \Delta T \left(z = 0\right) \sqrt{4\pi Dt}\,, \tag{4.12}$$

Our analysis uses Equation 4.12 because our measurement system naturally integrates any phase measured over a finite depth. This depth contributes to the optical path length change due to the absorbed optical energy pulse. Note that, at $z = 0$, Equations 4.11 and 4.12 are related by a $(4\pi Dt)^{1/2}$ term. Although the temperature is theoretically larger at the time the laser pulse first hits, the path of length of the material affected is very small. Thus the measured phase distribution has reduced temporal dependence near the initial absorption event than one would expect from Equation 4.11.

To extract the exact temperature dependence, the phase distribution was converted to temperature. Table 4.3 shows the parameters we used with Equations 4.11 and 4.11 for our theoretical model. Some data was not available from the slide distributor (Ted Pella, Inc.) and this was estimated from similar glasses from Industrial Glass Tech, Inc. and in [108, 107], which were also phase measurement studies of laser absorption. The phase distribution was not imaged in these works, but they provided useful guidelines for our measurement. The phase data was assumed to be primarily due to thermal effects

Table 4.3: Sample parameters

Symbol	Parameter	Value	Units
A_{tot}	Total absorption[a]	0.1	%
n_s	Refractive index (at 546 nm)[b]	1.517	–
α_s	Coefficient of thermal expansion[b]	90.6×10^{-7}	K^{-1}
ν_s	Poisson's ratio[b]	0.2	–
ρ_s	Mass density[b]	2.48×10^{3}	kg m^{-3}
c_s	Specific heat capacity[c]	880	J kg^{-1} K^{-1}
D_s	Thermal diffusivity[d]	4.6×10^{-7}	m^2 s^{-1}
$(dn/dT)_s$	Thermo-optic coefficient[e]	2.06×10^{-6}	K^{-1}
$(ds/dT)_s$	Change in path length with temperature[d]	2.1×10^{-6}	K^{-1}
t_f	Film thickness[a]	300	nm
f_{cam}	Camera frame rate	11800	fps

[a] measured.
[b] Ted Pella, Inc. technical note.
[c] Industrial Glass Tech, Inc. technical note.
[d] [106]
[e] [107]

at the surface of the sample. However, the physical quantities in question were assumed to be primarily due to the substrate. We assumed that the film contributed negligible effects, other than some optical absorption, due to its small thickness (300 nm) compared to the thermal penetration depth (4 microns at 10 microseconds). We measured the total optical absorption at 1064 nm to be 0.1 % with our photothermal common-path interferometry system. Our theoretical framework is shown in the schematic in Figure 4.3. The difference in temperature caused by the pulse results in a path length change in the sample, which in turn produces a phase shift in the probe beam compared to the reference arm of the MZI. We took into account that absorbed optical energy affects the optical path length in two ways: thermal expansion and change of refractive index with temperature. These relations are expounded in Equations 4.13-4.16.

$$\Delta\phi_{tot} = \frac{2\pi}{\lambda}\left[\int_{film}\left(\frac{ds}{dT}\right)_f \Delta T\, dz + \int_{sub.}\left(\frac{ds}{dT}\right)_s \Delta T\, dz\right] \tag{4.13}$$

$$\Delta\phi(t) = \frac{2\pi}{\lambda}\int_{path}\left[(n_s-1)(\nu_s+1)\alpha_s + \left(\frac{dn}{dT}\right)_s\right]\Delta T(z,t)\, dz \tag{4.14}$$

$$\int_{path}\Delta T\, dz\Big|_{r=0} = \frac{\Delta\phi(t)/(2\pi/\lambda)}{(n_s-1)(\nu_s+1)\alpha_s + (dn/dT)_s} \tag{4.15}$$

$$\Delta T(t) = \left(\int_{path}\Delta T(z,t)\, dz|_{r=0}\right)/\sqrt{4\pi Dt} \tag{4.16}$$

If s is the optical path length of the MZI sample arm, Equation 4.13 shows a total phase change due to thermal path length changes in the film, (ds/dT)f, and in the substrate, (ds/dT)s. The temperature in each region is integrated. However, as was previously mentioned, because the film is so much thinner than the thermal penetration depth in the substrate and its absorption is relatively low, we neglected the film term in our analysis. Should the film terms in Equation 4.13 increase, in a multilayer film, for example, the phase-to-temperature relationship would be a more complicated sum of film and substrate, expansion and dn/dT effects. Equations 4.14 and 4.15 show our method of converting phase to integrated temperature and equation 4.16 shows the relationship between integrated temperature and our original distribution in 4.11. The values used for heating due to expansion and refractive index change were both on the order of 2 ppb per 1 °C. Therefore, the peak phase deviations of 1 radian at t = 10 μs correspond to temperatures of 1700 °C. This is rather large, but becomes reasonable when one considers that the absorbed pulse energy density is approximately 1010 J/m^3. This matches well with the exact evaluation of 4.11 at r = z = 0, and t = 10 μs with the substrate terms in Tables 4.1 and 4.3, which is 1800 °C.

4.4 Results

Figure 4.6 shows four successive frames out of a 100-frame measurement following 16 pump pulse cycles. The associated multimedia file, Visualization 1, sequences these images. With this data, we were in a position to test our theoretical framework. We used Equations 4.11 and 4.11, along with the parameters in Tables 4.1 and 4.3, to analyze our data spatially and temporally. Therefore, independent temperature measurements

were not necessary to find meaningful quantities from the phase data. As shown in Figures 4.1 and 4.3, we aligned the pump and probe beams such that both focal points occurred at the sample surface. After doing this, we observed faint periodic deviations in the video composed of consecutive high-speed interferogram frames, as shown in Figure 4.6. After processing, we observed periodic phase waveforms closely corresponding to the Gaussian shape given by theory. Clearly evident in Figure 4.6 is the central phase displacement in the first frame, which decays over the next three. Additionally, there is very little wave propagation evident in the radial direction. The wave appears to simply decay with relatively small radial expansion. Looking to Equation 4.11, this implies a beam area that is slightly wider than the diffusivity multiplied by time over the lifetime of the wave. These initial observations were investigated further.

4.4.1 Temporal data

We plotted the center point of the thermal waves over time - i.e. the point at the peak of Figure 4.6 (a). Due to the nature of the experiment, phase measurements were a sum of effects through a finite depth of the sample. Therefore, it was appropriate to fit the data to the integral of the temperature distribution, as in Equation 4.12. Figure 4.7 shows temporal data at the center of the beam fit with a least squares fitting algorithm, using Equation 4.12. The fitted parameter produced a thermal diffusivity of 5.4×10^{-7} m^2/s which is in agreement with the substrate diffusivity in Table 4.3.

4.4.2 Spatial data

Cross-sectional data from the images in Figure 4.6 are shown in Figure 4.8. This data shows that while the beam spread with time was small, it was measureable. Further analyzing Equation 4.11, a beam-area time-dependence can be observed in the argument of the r-term.

$$w^2(t) = w_0^2 + 2Dt \tag{4.17}$$

Where w is the beam waist. The spread of the thermal wave in the frames was found by extracting a 1D cross-section that intersected the same peak point used in the

temporal analysis. This data slice was fit to a Gaussian function and the waist of this Gaussian used as the waist of a fit to Equation 4.11 integrated over the optical path.

Figure 4.8 shows that the shape of the absorbed energy is Gaussian in the radial direction, as predicted by Equation 4.11, and that it expands with time. The initial beam waist of 18 microns in Figure 6 (a) expanded to 21 microns, in (b), in the time between energy absorption and the first frame. It further expanded to 23 (c), 25 (d) and 27 microns (not shown) in the three successive frames. Fitting the square of the beam waist to Equation 4.17 produces a diffusivity of 5.3 $\times 10^{-7}$ m^2/s. This linear fit is shown in Figure 4.9.

4.5 Discussion

It should be noted that the phase measurements were made relative to a reference point in the lower left corner of the frame (see Figure 4.6). The absolute phase of the frames varied strongly due to noise in the optical system. Subtracting a small reference region removed this overall frame noise while allowing us to glean physical data from within the frame. However, as the thermal wave expanded and entered the reference region an error term entered the measurement. This term was negligible in the first few frames of a pulse event, but became important as the frames accumulated as shown in Figure 4.10. This appeared in the temporal measurements and also complicated to the spatial measurement. Additionally, there was finite noise due to imperfections in the optical system. Some of this noise remained after reference point subtraction. This contributed to the temporal measurement and absolute temperature conversion, but was easily averaged over the spatial measurement. Finally, the lens system we used produced a finite distribution (i.e. the fringes were not perfectly straight). This produced no noticeable effects and the fringes appeared straight enough for our purposes.

The first frame of the temporal fit was assumed to be coincident with a frame of the measurement. In reality, there was a finite delay between the pulse absorption event and the first frame of the measurement. As a worst case this delay could have been up to a full frame of 87 s. Jitter analysis showed that the diffusivity fit varied strongly with the delay and was up to an order of magnitude larger in the worst case of being off by a full frame. However, our camera measurement was electronically triggered with a gate

signal, which also triggered the laser. The trigger delay was not likely more than 1 s and our data fit produces accurate results, so our assumption appears to be reasonable.

4.6 Conclusion

We designed a high-speed monitoring system capable of imaging the dynamic temperature distribution of a laser-irradiated sample. This high-speed phase setup allows in situ thermal monitoring of optical components and control of laser processes as well as phase data on any catastrophic event that may occur. When comparing our data to a theoretical estimate we needed values for absorbed energy density and heat capacity. We assumed the heat capacity of the sample was identical to literature values. We measured the absorption with our photothermal common-path interferometry system to be 0.1%. Using Equations 4.11 and 4.12 and values in Tables 1 and 2 produced theoretical temperatures very close to experimental temperatures on the order of 1700 degrees Celsius. However, we were able to extract thermal diffusivity from the phase data without exact temperature calibration. We captured multiple frames and were able to track the thermal wave with time. We deconvolved the interferograms and tracked the center point of the temperature distribution temporally. We also tracked a 1D slice of the thermal distribution with time. We fit our phase data to 4.11 and 4.12 to produce similar thermal diffusivity values of approximately 510-7 m2/s. Our extracted value of thermal diffusivity was in excellent agreement with known values from literature.

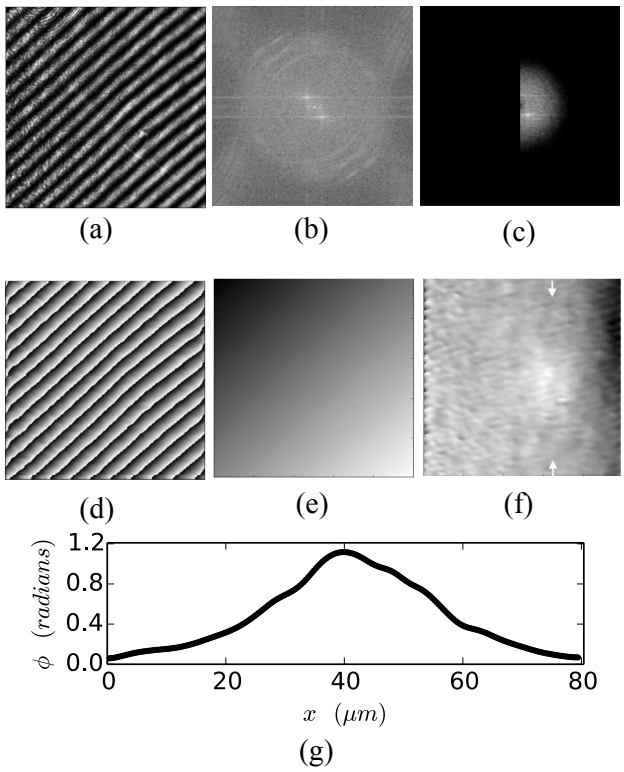

Figure 4.2: Phase post-processing of an interferogram taken immediately (within 1 frame or <84 s) after an Nd:YAG pulse. Starting with (a) an interferogram, the image is (b) Fourier-transformed, (c) band-pass filtered and negative frequencies are removed. An inverse Fourier-transform without these negative frequencies results in a Hilbert transform. The argument of the now complex data is (d) the phase image. The phase is (e) unwrapped and (f) the fringe bias is removed to give the phase image of the sample. (g) a quantitative phase cross-section is indicated by the arrows in (f). This pulse shape shows a Gaussian profile, which decayed and expanded with time - typical of thermal phenomena. All frames are 100 microns square.

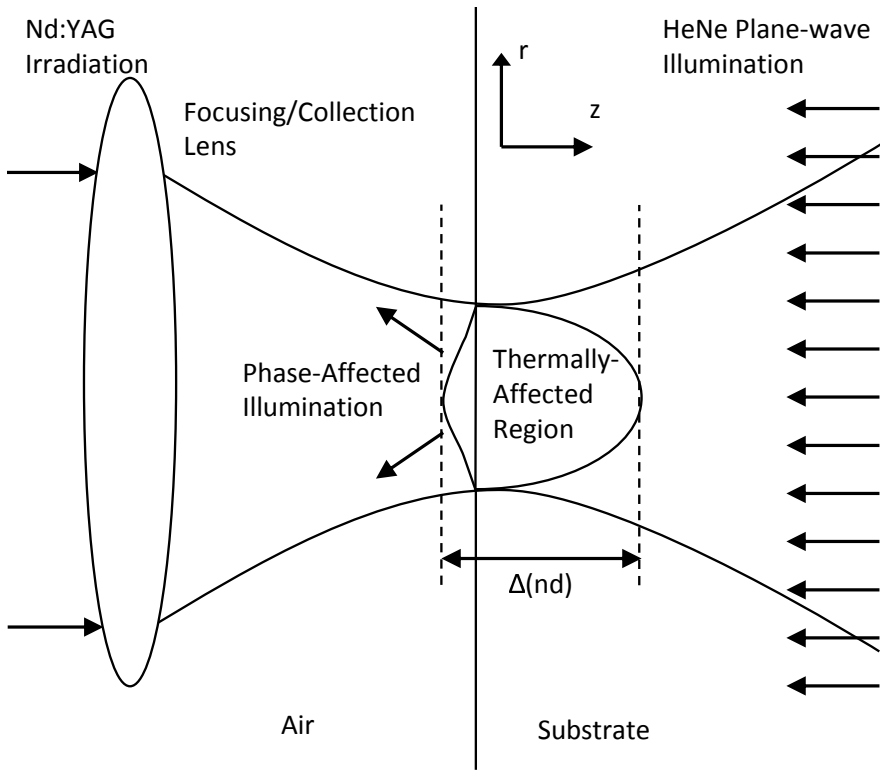

Figure 4.3: Diagram of theoretical model. Energy from the pulsed Nd:YAG laser is focused to a spot on the sample surface. Absorbed energy causes material effects, which produce an optical path-length change, Δ(nd), which produced a phase shift in the HeNe pseudo-plane-wave back-illumination. The phase-affected light is collected by the same focusing lens and carried to the imaging system which records the phase shift via a reference beam from the same HeNe illuminating laser. Coordinates r and z from Equations 4.11 and 4.12 are shown.

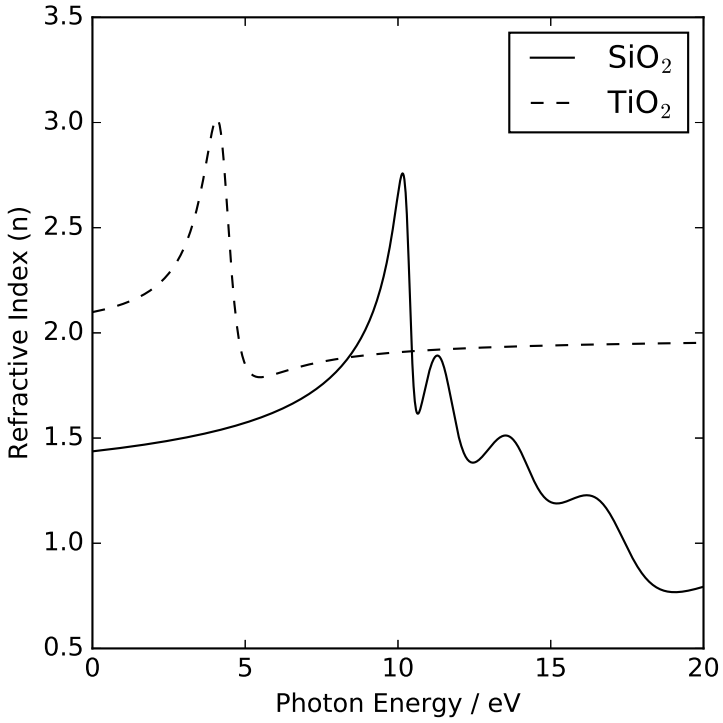

Figure 4.4: Refractive index spectrum calculated from Equation 4.5 using parameters for SiO_2 and TiO_2. The spectrum shows increased sensitivity near the bandgaps of $E_g = 7.0$ eV and $E_g = 3.0$ eV, respectively.

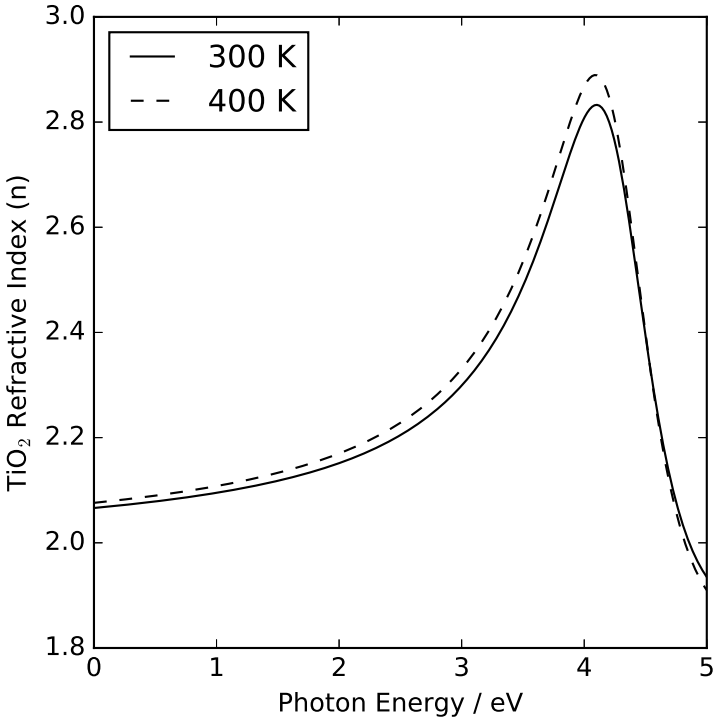

Figure 4.5: Refractive index spectrum for TiO_2 at 300 K and 400 K, calculated with values after [104].

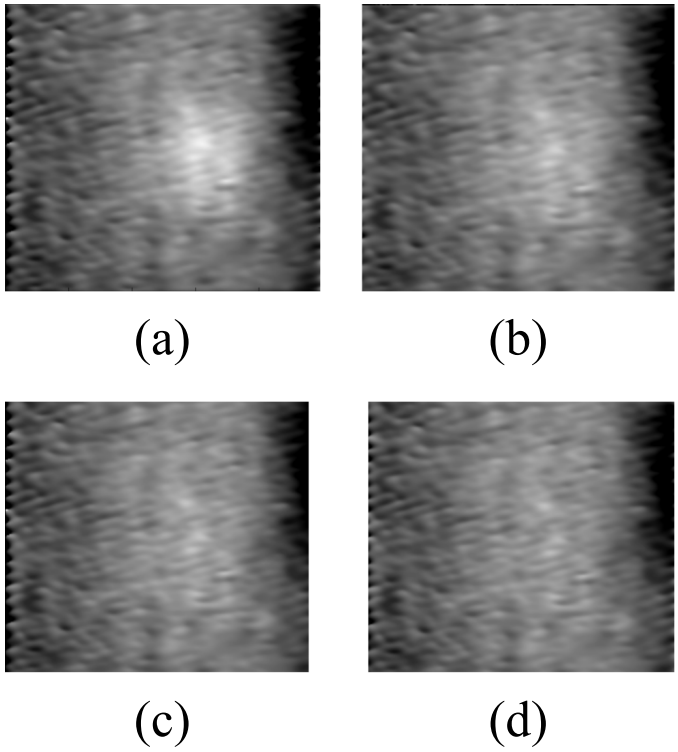

Figure 4.6: Temporal phase phenomena observed on yttria-coated glass slide. The first frame (a) is the closest frame captured after the laser pulse was absorbed by the sample. Frames (b)-(d) show this initial pulse dissipating. Frames are 100 microns square.

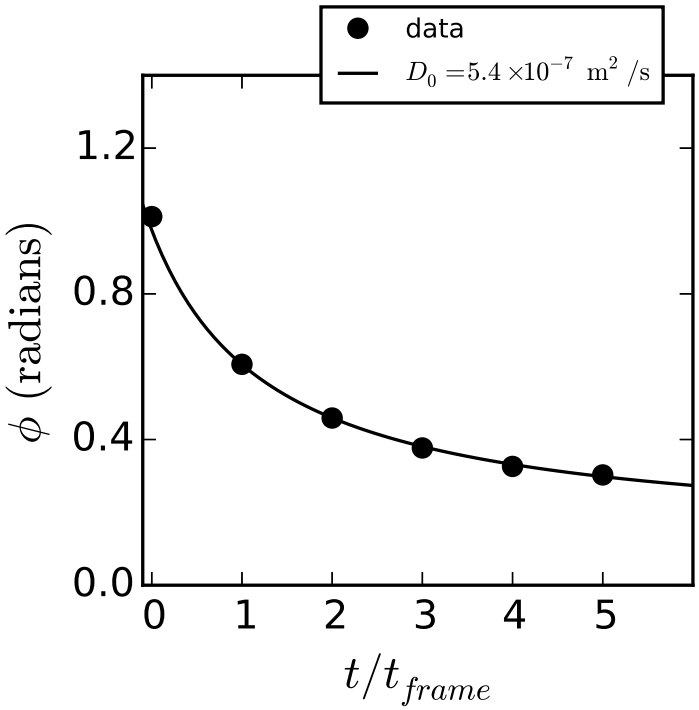

Figure 4.7: Temporal decay of the temperature pulse. Data taken at the center of the temperature distribution. Also shown is a solid depicting a fit using (2). The diffusivity fit is in good agreement with literature values. The frame-rate here was 11,800 fps, which corresponds to a frame period of 84.7 μs.

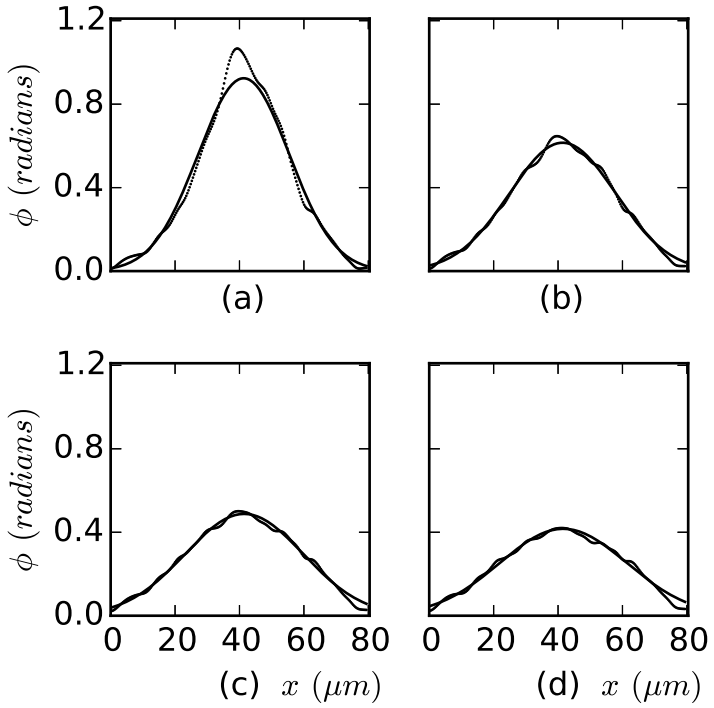

Figure 4.8: Radial temperature distribution in the four frames captured immediately after the laser pulse. The beam waist was quantified by fitting a Gaussian function (solid line) to the data (points). Subfigures (a-d) show fits from four successive frames.

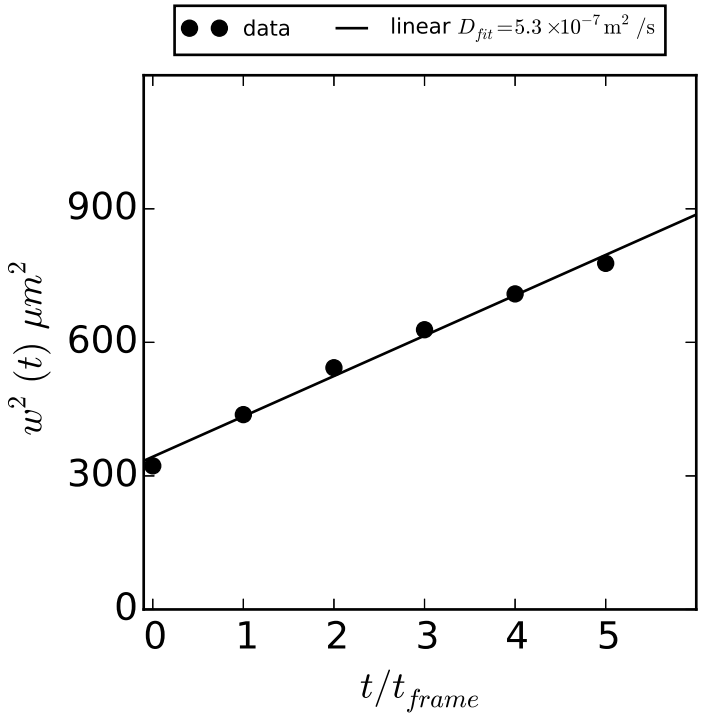

Figure 4.9: Fitted Gaussian widths-squared from Figure 4.8, plotted against time. A thermal diffusivity can be extracted from a linear fit to this data, according to Equation 4.16.

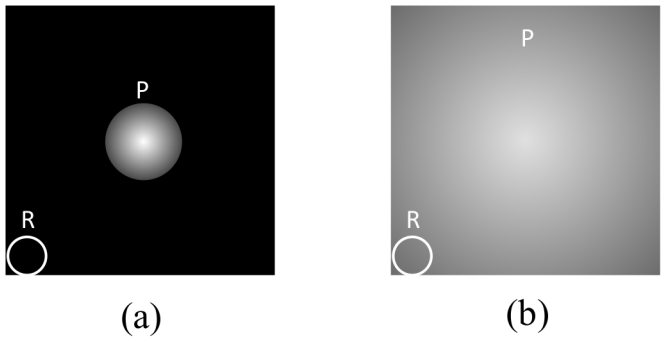

Figure 4.10: Accumulation error demonstrated with mock example phase frames. In (a) the absorbed laser pulse energy, P, is far from the reference region, R and the reference region can be safely subtracted to remove any absolute noise in the frame. In (b) the pulse energy has spread into the reference region and the frame will be incorrectly referenced.

Chapter 5

Subsampling Phase Retrieval

5.1 Introduction

The previous study outlined an experimental system for the capture of thermal processes during laser damage events. Such a measurement could conceivably be a part of a real time laser damage monitoring system. However, in our system, the thermal information was contained in the optical phase field, which must be retrieved by a mathematial technique. This technique can take some time and the overall measurement time is limited by this. Therefore, work was done to develop a phase retrieval system that could recover thermal information as fast as it is recorded[109]. We demonstrate a interferogram-subsampling phase-retrieval technique with improved speed performance over other techniques. Subsampling is a common technique in radio phase detectors and can offer power improvements because of the reduced sampling frequency [110]. Our simple thermal measurement system comprises a Mach-Zender interferometer combined with a magnification loop. Interferograms are recorded with a high-speed camera and data is acquired and processed via computer. Such a system has found use for laser damage experiments [91]. In addition, high-speed temperature imaging could find use for thermal monitoring of electronic circuits [111] and electromigration [112]. Fast optical phase retrieval for thermal monitoring as a part of a control loop could prevent thermal runaway in complex electronic and photonic systems. Finally, thermal interferometry for materials studies has a rich history from scattering techniques like thermal lensing [106] to thermal interferometric and holographic methods [113]. Improving the speed

response of thermal imaging systems could open the door to new applications in materials studies. Recently, quantitative phase interferometry has had a renewed interest for biological applications [114]. There is a similarity between thermal measurements in transparent optical systems and measurements transparent biological systems. We have been able to take advantage of the recent biological developments for our work. We developed a inteferometric microscope from a Mach-Zender interferometer and magnification loop. Prior art for phase retrieval in such a system is as follows. In [115], a fast and simple computational technique was used to retrieve an analytic signal from fast fourier-transform (FFT) data. This technique had 21.2 nm of spatial noise. Here we use the term spatial noise to mean the standard deviation of the 2D phase map, converted to surface optical thickness units. In [116] a fast Hilbert method was used to retrieve a 2D phase map and to record 2D phase maps over time. The spatial noise of their retrieval system was less than 100 nm. The temporal noise of the phase map was averaged over the diffraction limited spot of the imaging system on the phase map. The standard deviation or temporal noise of this measurement was 1.32 nm. Other workers modified a similar system to remove residual phase error [117, 118]. Their system had between 10 and 50 nm of spatial noise. Still other workers developed a system which differentiates refractive index from absolute thickness by use of two different ambient media [119]. This system had under 12 nm of spatial noise. Our method matches this noise performance, but it exceeds in speed and drift performance. Our system had a temporal noise of 8.62 nm and a spatial noise of 16 nm. While high SNR is required for biological imaging, heat transfer analysis and thermal monitoring may have less stringent noise requirements. The trade-off for more speed may be advantageous.

5.2 Measurement system

Our measurement Mach-Zender interferometric microscope was described in previous work [91]. We modified the system with balanced confocal magnification loops in each arm, with 10x magnification. We neglected a condenser lens prior to the sample for simplicity. The resulting quadratic phase field in the image plane was found to be small. Our system was calibrated with an aluminum resistor sputtered on a glass substrate. The aluminum linear temperature coefficient of resistivity (TCR) was measured as 0.25

%/K. Equation 5.1 shows the resistance-to-temperature conversion:

$$R(\Delta T) = R_0 \left(1 + \alpha \Delta T\right) \tag{5.1}$$

where α is the TCR, R is the resistance, R_0 is the room temperature resistance and ΔT is the change in temperature from room temperature. R_0 was measured as 400 Ω. The aluminum resistor was contacted by micropositioner probes connected to a Keithley 2120 sourcemeter. This allowed us to simultaneously source power through the resistor and measure the change in resistance with temperature. The Keithley sourcemeter was software controlled through a GPIB interface. The software control program also triggered and retrieved frames from the high-speed camera and triggered both instruments for measurement. Our measurement consisted of a 2-volt, 50 ms pulse from the sourcemeter. We measured the current in the resistor continuously before, during and after the pulse. We also recorded interferogram frames before, during and after the pulse. The software control program timed all of the measurements so that we could correlate measured changes in resistance (due to temperature) with measured changes in optical phase (also due to temperature).

5.3 Algorithm

Our interferogram can be considered to be the product of a complex object wave with the phase information of interest and a complex reference wave [120, 121, 122]:

$$I = R^2 + O^2 + R^* O + R O^* \tag{5.2}$$

where I is the interferogram, R is the reference wave and O is the object wave carrying information from the sample. Here, R^* refers to the complex conjugate of a wave, R. Mathematically, the interferogram can be represented by the following. For simplicity, only one dimension is given, but in practice the interferogram is two dimensional:

$$I(x) = I_0 \left[1 + a \sin(kx + \phi(x))\right] \tag{5.3}$$

where I_0 is the mean intensity, a is the inteferogram amplitude, k is the spatial frequency and ϕ is the phase function of interest. For sine-like interferograms, our phase

retrieval algorithm basically consists of sampling this sine function near its zero-crossing. It is well-known that for $\theta \ll 1$, $\sin\theta \approx \theta$. In addition, we used both positive-going zero-crossings and negative-going zero-crossings by multiplying the negative-going by -1. Therefore, the problem of phase retrieval is reduced to generating a sampling lattice of the zero-crossings of a reference interferogram (without any phase perturbations), and sampling frames with this lattice during experiments. Subsampling should not break the Nyquist criterion for the phase object if the frequency of the interferogram is much higher than the bandwidth of the phase object of interest. Figure 5.1 shows an example interferogram –without any sample heating– being prepared as a reference from which a subsampling lattice may be generated. This is done by processing the interferogram for the carrier wave via Fourier-transform, filtering and inverse transform steps.

After that, the gradient is generated and a peak-finding algorithm applied to find the peaks of the gradient, which correspond to the zero-crossings. These points are saved in a sampling lattice. Figure 5.2 shows a sample lattice generated with real data. The data shown is a subset of that in Figure 5.1d.

In practice, we collected all the interferograms of the experiment at once and processing was done afterward. The first frame in the measurement contained no temperature-dependent data of interest, and was used as a reference interferogram for generating the sampling lattice. The sampling lattice was generated as follows. The interferogram was first high-pass filtered to remove the zero-order holographic components. Then, the 2D gradient of the data was taken. Zero-crossings in sine-data have maximum slope and thus will produce local maxima in gradient data. A one-nearest-neighbor peak-finding algorithm was then applied and the peaks were saved as a masking array. The peak-finding algorithm differentiated between negative and positive peaks and generated a separate mask for each. This mask set was then applied to the frames generated during resistor heating. From a measurement standpoint, once the sampling lattice was generated, phase retrieval is only limited by how fast frames can be retrieved from the camera for processing. In a live setting, camera frames could concievably be subsampled for feature extraction as a part of a thermal monitoring control loop. Such a loop could prevent thermal runaway in electronic systems. For the purposes of visualization, all non-mask points in the frame were set to zero. This allowed us to view the effect

of heating on the sampling lattice. We found, for our measurements, that the subsampling method corresponded very well with traditional holographic and Hilbert-transform methods. Figure 5.3 shows a sample retrieval process as well as a comparison between a smoothed, subsampled phase image and a phase image retrieved by Hilbert-transform.

5.4 Speed

Once a sampling lattice is generated, our sampling algorithm could proceed as fast as frames are retrieved from the camera. In comparison, our Hilbert-transform system had a phase retrieval speed of 66 ms on a 2012 Apple MacBook Air. Our Hilbert-transform algorithm required an FFT. Our FFT speed was 6 ms and the inverse-FFT speed was 11 ms. By subsampling the image data in computer memory, phase data could be retrieved in under 1 ms for a speedup of over 66. By subsampling data from the camera directly, even greater speeds could be realized.

5.5 Thermal data

The visible temperature distribution in the substrate was calculated from analytical techniques in Carslaw & Jaeger [90][Carslaw & Jaeger]. A Green's function analysis was used to calculate the temperature distribution in 2D image space. Importantly, any phase-imaging system will integrate the phase response over the optical path. We assumed that the integration distance was much longer than the thermal perturbation distance. A starting point for the Green's function analysis is the Green's function solution itself, for an impulse of heat:

$$G(x, y, z, t) = \frac{Q}{\rho c (Dt)^{3/2}} \exp\left[-\frac{x^2 + y^2 + z^2}{4Dt}\right] \tag{5.4}$$

Here, G is the increase in temperature in time and space due to an impulse of energy Q at the origin. The diffusivity of the medium is D with density and heat capacity ρ and c. The Green's function analysis proceeds by integrating the impulses over time and space according to the source distribution. This can be modeled as a convolution operation:

$$u(x,y,z,t) = \int dx_0\, dy_0\, dz_0\, dt_0\ [S(x,y,z,t)G(x-x_0, y-y_0, z-z_0, t-t_0)] \tag{5.5}$$

In essence, this is distributing a number of impulses over all the locations the source is present. For our analysis, we will actually begin by integrating over the optical path, L:

$$u_1(x,y,t) = \int_{-L}^{L} G(x,y,z,t)\ dz \tag{5.6}$$

$$u_1(x,y,t) = \frac{Q}{\rho c D t}\mathrm{erf}(L/\sqrt{Dt})\exp\left(-\frac{x^2+y^2}{4Dt}\right) \tag{5.7}$$

Next we integrate source terms over the line heater in the y-direction for a heater of length b:

$$u_2 = \int_{-b}^{b} u_1(x, y-y', t)\ dy' \tag{5.8}$$

$$u_2(x,y,t) = \frac{Q}{\rho c\sqrt{Dt}}\mathrm{erf}(L/\sqrt{Dt})\left[\mathrm{erf}((y+b)/\sqrt{Dt}) - \mathrm{erf}((y-b)/\sqrt{Dt})\right]\exp\left(-\frac{x^2}{4Dt}\right) \tag{5.9}$$

Now we can let L and b go to infinity as they are much larger than the optical path and field-of-view respectively. This results in a simpler line-heater impulse-response:

$$u_3 = \frac{Q}{\rho c\sqrt{Dt}}\exp\left(-\frac{x^2}{4Dt}\right) \tag{5.10}$$

Finally, we want the solution to a step response, which requires convolution of u_3 with a step function:

$$u_4 = \int_0^t u_3(x, t-t')\ dt' \tag{5.11}$$

Therefore, the thermal response integrated over the optical path was found as follows:

$$\int \Delta T\, dz = \frac{q}{\rho c}\left[\exp\left(-\frac{x^2}{4Dt}\right)\sqrt{4Dt} - |x| + x\,\mathrm{erf}\left(\frac{x}{4Dt}\right)\right] \tag{5.12}$$

where q is the power delivered by the resistive heater, ρ is the substrate density, c is the heat capacity and D is the thermal diffusivity.

A fit of this equation to data is shown in Figure 5.4, and produced a thermal diffusivity of 5×10^{-7} m^2/s, which is consistent with that found in literature [91, 106]. It should be noted that generating a sampling mask also allowed us to mask regions of the sample with low transmission (i.e. regions blocked by the resistor). These regions were left out of the retrieval and data fitting, allowing us to produce a superior fit. The temperature of the resistor during the heating cycle was recorded by both the optical system and the sourcemeter. The peak temperature reached was 28 °C. A plot of the two temperature measurements is shown in Figure 5.5. Due to system limitations, temperature data recorded by the sourcemeter could not be recorded at the same rate as the high-speed optical system. However, the temporal shape of the two data sets are in agreement.

5.6 Discussion

Subsampling is a close-to-real-time technique which retrieves phase information by relying on a sine approximation. Concievably, a system could be built which generates a subsampling lattice and then only retrieves camera pixels on the lattice. Such a sampling scheme could be built with a field-programmable gate array (FPGA) as part of a high-speed thermal feature monitoring and control system. Obviously, this subsampling technique is most useful for very small phase signals, as large signals produce difficult wrapping errors. There may be some techniques for unwrapping these errors, but the subsampling scheme would be reduced in speed if an unwrapping step were required. It is interesting to note that our measurement showed air-heating effects after 200 frames. This is an example of interesting information that a real-time thermal monitoring system could produce.

5.7 Conclusion

We have demonstrated a useful phase measurement system with remarkable phase retrieval speed improvement. Our system is most useful for monitoring small thermal signals. We tested our system with a real experiment and found substrate thermal diffusivity in good agreement with published values.

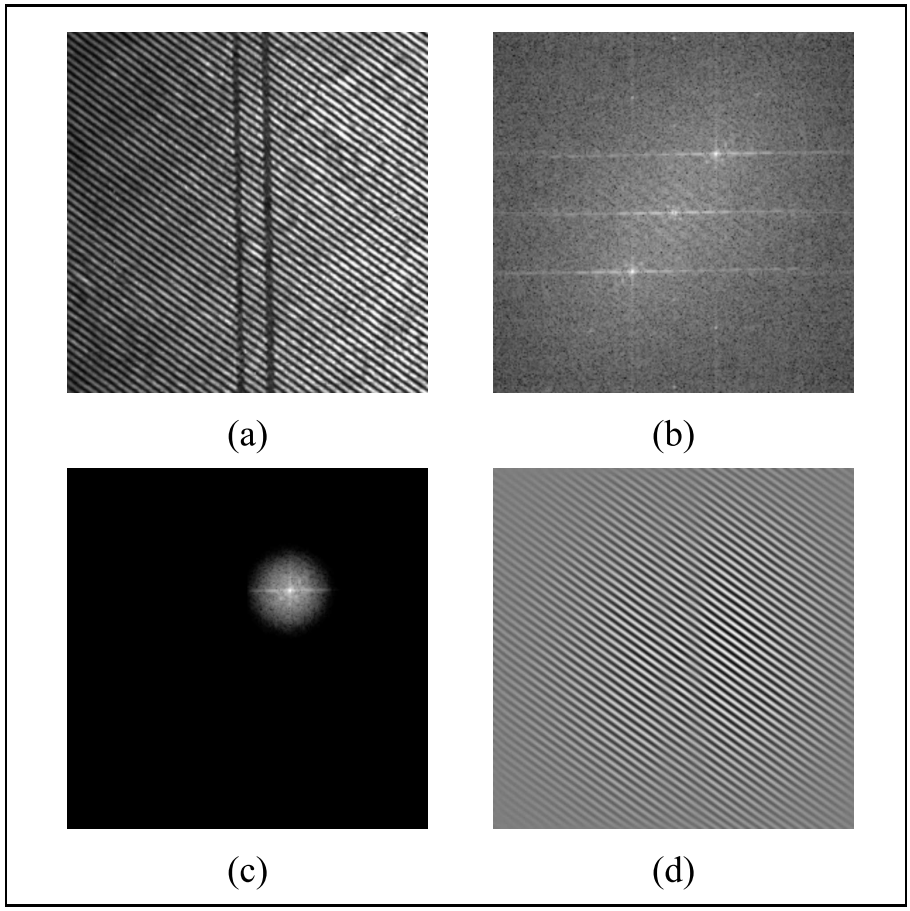

Figure 5.1: Generation of the reference field. Interferogram in the absence of heating (a) is Fourier-transformed (b) and filtered (c) to produce a reference field (d). Opaque lines on (a) are aluminum resistors. Subfigures (a) and (d) are 256 x 256 pixels and 1 mm x 1 mm.

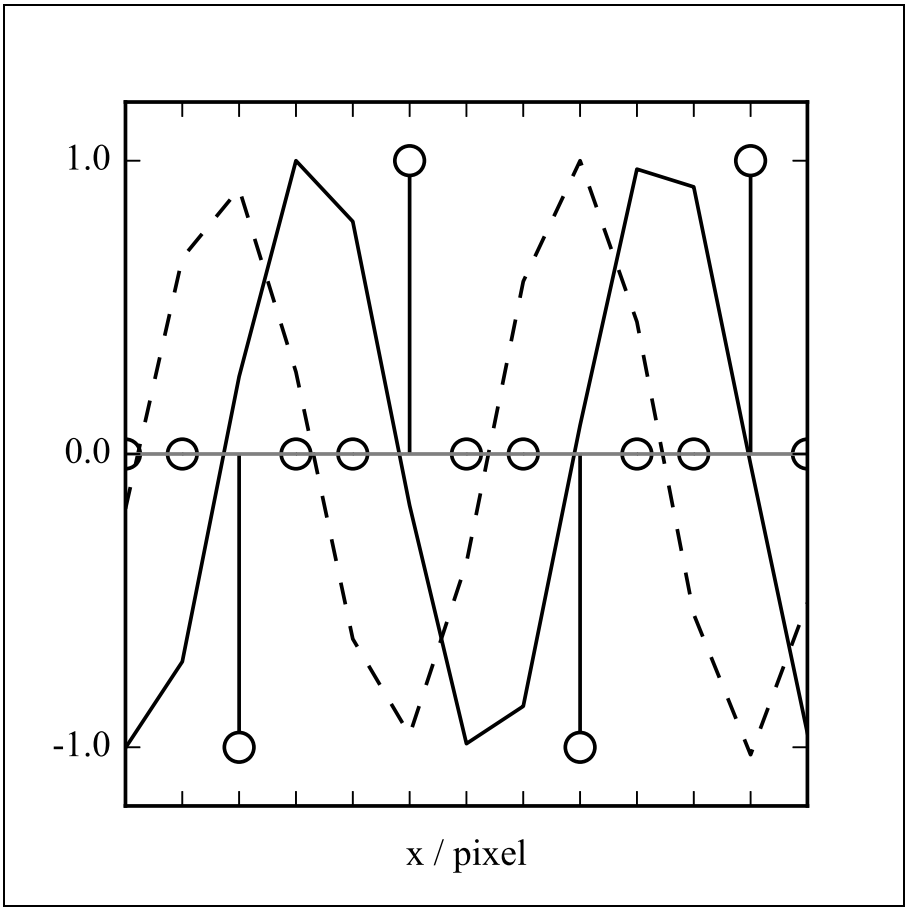

Figure 5.2: Generation of the sampling lattice. A slice of the real part of the reference field in Figure 5.1 has been shifted and normalized (solid line). To find the zero-crossings, the gradient was taken (dashed line). The sampling lattice is represented by circles with lines. A peak-fitting algorithm assigned +1 and -1 to the troughs and peaks of the gradient field, respectively. All other points were set to zero.

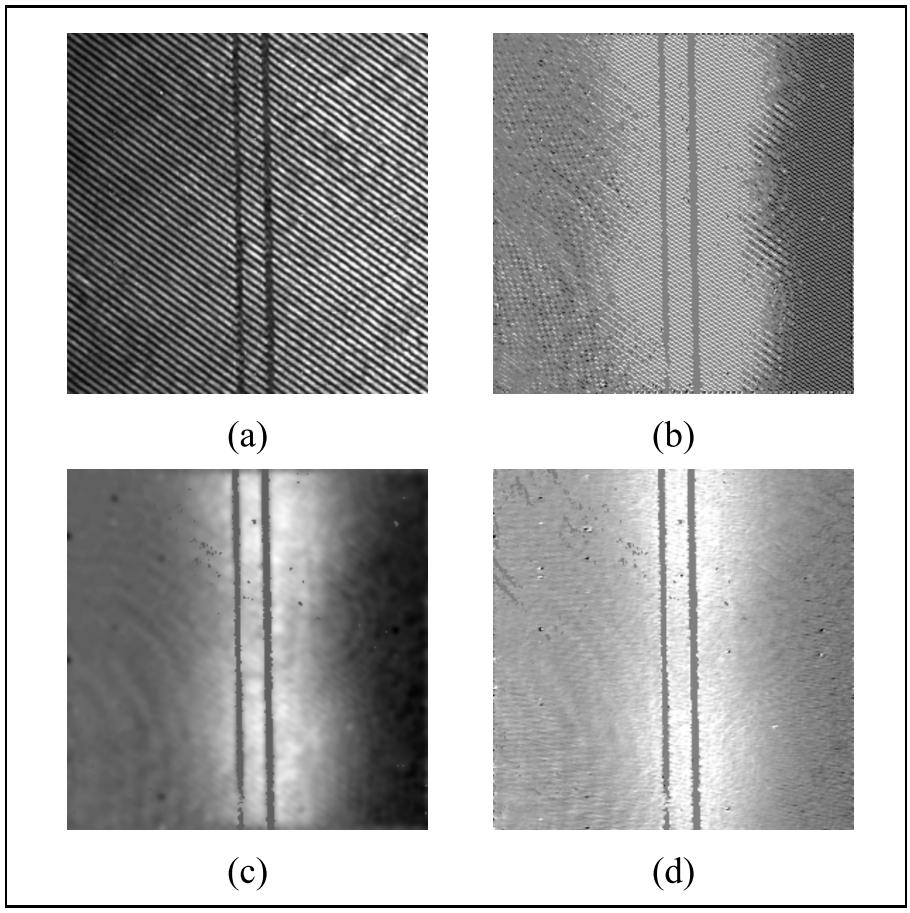

Figure 5.3: Phase retrieval by subsampling. An interferogram in the presence of heating (a) is sampled by the sampling lattice (b). A low pass filter is applied for better visualization (c). For comparison, phase retrieval by a Hilbert-transform method is shown (d). Scale is in arbitrary units. Brightest points in (c) and (d) correspond to approximately 1 radian optical phase. The opaque lines on the plots are the aluminum resistors. Subfigures are 256 x 256 pixels and 1 mm x 1 mm.

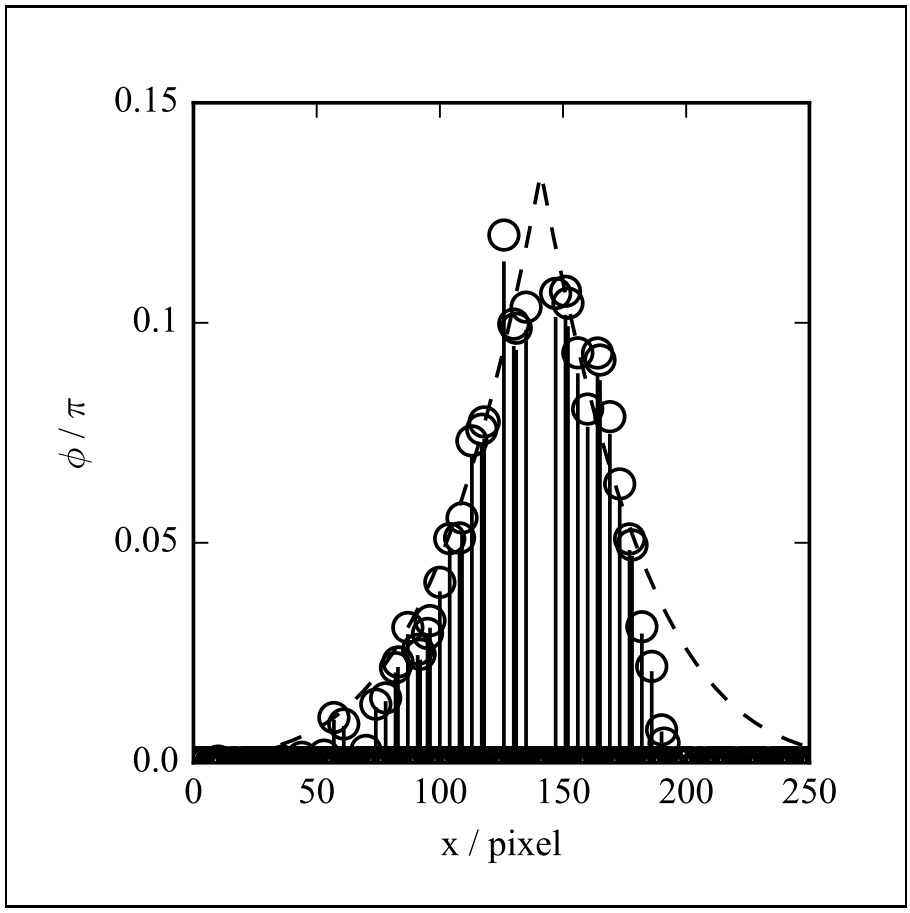

Figure 5.4: Thermal fit. The phase of a heated frame, shown in Figure 5.3c, was averaged along the y-dimension to produce a 1D phase distribution (open circles with lines). This data was fit using Equation 5.12 (dashed line). The fit produced a thermal diffusivity of 5e-7 m2/s, in excellent agreement with known values for soda-lima-silica glass. Fall off on the right side of the graph was attributed to intensity bias due to non-uniform illumination. Total x-axis length was 256 pixels and 1 mm.

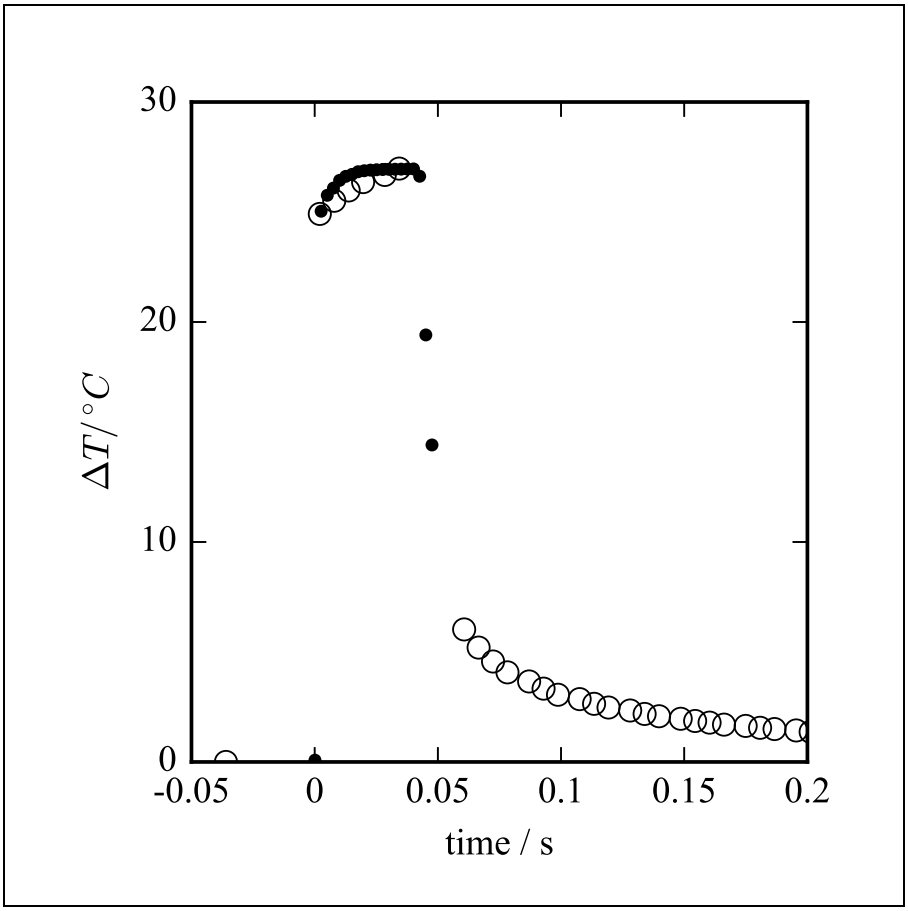

Figure 5.5: Temperature data vs. time. Temperature was recorded via aluminum resistor (open circles). Resistance was converted to temperature via Equation 5.1. These values were used to calibrate the phase data taken over time (closed points). Data sets were aligned temporally via software triggering during testing. This graph shows the agreement in the shapes of the temperature recorded by the camera and the resistor.

Chapter 6

Conclusion and Discussion

The optical analysis systems described in the previous chapters have allowed a better understanding of thermal deformation in optical and electronic media. Laser damage studies may benefit from the experimental and analysis techniques presented in this work. As a cohesive unit, this work presents theoretical background and experimental work on light-matter interactions in the high-power regime. The work has been presented from an electrical engineering standpoint, with the tools engineers use to understand materials and system design. In turn, this engineering work has informed our understanding of how nano-structured materials interact with light and how thermal waves dissipate through optical media.

The theoretical framework for this thesis was presented. This included a description of laser damage terminology, the optical materials considered, short pulse damage mechanisms and long pulse damage mechanisms. Short and long pulse damage mechanisms differ significantly in that the former is primarily field-induced, while the latter is thermal. Short pulse damage mechanism were explore as they present the fundamental field limits of the materials in question. Multiphoton ionization and impact ionization were presented as absorption and breakdown mechanisms. There is some dispute about the contribution and validity of impact ionization. Both mechanisms bear more theoretical and experimental work. Long pulse and CW damage was explored from a laser-heating perspective. Models for laser heating of materials were presented. This was followed by a detailed exploration of thermal expansion and its effect on laser damage.

After presenting the theoretical framework, a first study was described. This laser

damage experiment compared the laser damage resistance of two types of films: a nanolaminate film and a uniformly grown film. The nanolaminate film was composed of a uniformly grown film with spaces of amorphous film. This prevented crystal grain formation in the film. While previously thought to reduce scattering and thus have better short-pulse laser damage performance, the amorphous film had reduced CW laser damage performance. This was thought to be due to the reduced thermal conductivity of the film. The reduced thermal conductivity of the film was verified by the three-omega method. We did tests on hafnia and titania films. The uniformly-grown polycrystalline hafnia films had a thermal conductivity of 1.72 W/m-K, while the nanolaminate hafnia films had a thermal conductivity of 1.02 W/m-K. The titania films had similar results. We developed a theoretical model that explained why nanolaminate films perform better for ns testing, but worse for CW testing. Our model was based on the relative absorption and thermal conductivity of the films in question. In addition, we observed bull's-eye damage features in some of the tests. These features occured in some of the uniform hafnia and nanolaminate hafnia tests. We analyzed these features and found that they fit Bessel functions very well. Bessel functions are solutions to heat transfer partial differential equations as well as mechanical systems of equations for radially-symmetric systems. However, our model did not agree with known properties of thermal diffusion waves. These, interesting damage morphologies led us to pursue a thermal analysis further.

We developed a high-speed imaging system capable of capturing thermal events in the optical samples. The system was designed as a Mach-Zender interferometer with a microscope objective. In the sample arm, a laser heated optical glass substrate was placed. The laser events were recorded with a high-speed camera capable of capturing events at up to 20,000 frames per second. We observed thermal events via the thermo-optic effect. The theory for this effect was presented. Using our heat transfer theoretical framework we fit thermal data captured with the interferometer to our model. The fits produced thermal diffusivity on the order of 5×10^{-7} m^2/s. This is in good agreement with other works on similar substrates.

Our high-speed imaging system allowed us to caputure thermal data after post-processing. We desired a system that could present thermal data to a monitor or to a control loop much faster. Our initial algorithm used a Hilbert-transform method to

produce phase images. Our Hilbert-transform method required two time-consuming fourier-transform steps. We developed a convolution method with a small convolution kernel, which could potentially be faster. However, the greatest speed improvement came with the development of a subsampling technique that used the small-angle approximation to sample points of the interferogram close to the zero-crossing of the constituent sine-wave. Our subsampling technique had 16 nm of spatial noise, comparable to state-of-the-art. However, the retrieval time was 60x faster than our previous method. Therefore, our system could truly retrieve thermal information in real time.

To further explore this work, it would be interesting to explore thermal models of optical systems with defects or absorbing centers. In addition, such a sensitive instrument could be applied to the study of non-linear light-matter coupling in high-intensity experiments. It would be interesting to record the differing thermal conductivities of the films studied first. Experiments could potentially show which films would have the best laser damage performance without actually damaging them. The high-speed phase retrieval could be an element of a control loop to run the test.

In summary, this work showed a tradeoff between coatings with low absorption and low thermal conductivity in short- and long-pulse regimes; a successful high-speed imaging and modeling technique motivated by unique morphologies observed in the first study; and a faster image processing technique capable of capturing thermal data in real-time. These experiments and methods will be useful for designing and monitoring optical materials in high-power laser systems.

References

[1] J. H. Cullom and R. W. Waynant. Determination of Laser Damage Threshold for Various Glasses. *Applied Optics*, 3(8):989–989, August 1964.

[2] Roger M. Wood. *Laser-Induced Damage of Optical Materials*. CRC Press, Bristol, 1 edition edition, August 2003.

[3] David W. Camp, Mark R. Kozlowski, Lynn M. Sheehan, Michael A. Nichols, M. Dovik, Robert G. Raether, and Ian M. Thomas. Subsurface damage and polishing compound affect the 355-nm laser damage threshold of fused silica surfaces. In *Laser-Induced Damage in Optical Materials: 1997*, pages 356–364. International Society for Optics and Photonics, 1998.

[4] W. Lowdermilk and David Milam. Laser-induced surface and coating damage. *IEEE Journal of Quantum Electronics*, 17(9):1888–1903, 1981.

[5] Andrew C. Tam, Wing P. Leung, Werner Zapka, and Winfrid Ziemlich. Laser-cleaning techniques for removal of surface particulates. *Journal of Applied Physics*, 71(7):3515–3523, 1992.

[6] B. C. Stuart, M. D. Feit, A. M. Rubenchik, B. W. Shore, and M. D. Perry. Laser-Induced Damage in Dielectrics with Nanosecond to Subpicosecond Pulses. *Physical Review Letters*, 74(12):2248–2251, March 1995.

[7] WJ Padilla DR Smith. Composite Medium with Simultaneously Negative Permeability and Permittivity. *Physical Review Letters*, 84(18):4184–7, 2000.

[8] John Brian Pendry. Negative refraction makes a perfect lens. *Physical review letters*, 85(18):3966, 2000.

[9] R. A. Shelby, D. R. Smith, S. C. Nemat-Nasser, and S. Schultz. Microwave transmission through a two-dimensional, isotropic, left-handed metamaterial. *Applied Physics Letters*, 78(4):489–491, January 2001.

[10] R. A. Shelby. Experimental Verification of a Negative Index of Refraction. *Science*, 292(5514):77–79, April 2001.

[11] David R. Smith, John B. Pendry, and Mike CK Wiltshire. Metamaterials and negative refractive index. *Science*, 305(5685):788–792, 2004.

[12] Ta-Jen Yen, W. J. Padilla, Nicholas Fang, D. C. Vier, D. R. Smith, J. B. Pendry, D. N. Basov, and Xiang Zhang. Terahertz magnetic response from artificial materials. *Science*, 303(5663):1494–1496, 2004.

[13] John B. Pendry, David Schurig, and David R. Smith. Controlling electromagnetic fields. *Science*, 312(5781):1780–1782, 2006.

[14] David Schurig, J. J. Mock, B. J. Justice, Steven A. Cummer, John B. Pendry, A. F. Starr, and D. R. Smith. Metamaterial electromagnetic cloak at microwave frequencies. *Science*, 314(5801):977–980, 2006.

[15] Viktor G Veselago. The Electrodynamics of Substances with Simultaneous Negative Values of ϵ and μ. *Soviet Physics Uspekhi*, 10(4):509–514, April 1968.

[16] Ilya V. Shadrivov, Alexander B. Kozyrev, Daniel W. van der Weide, and Yuri S. Kivshar. Tunable transmission and harmonic generation in nonlinear metamaterials. *Applied Physics Letters*, 93(16):161903, 2008.

[17] Bingnan Wang, Koon Hoo Teo, Tamotsu Nishino, William Yerazunis, John Barnwell, and Jinyun Zhang. Experiments on wireless power transfer with metamaterials. *Applied Physics Letters*, 98(25):254101, 2011.

[18] Don Shiffler, John Luginsland, David M. French, and Jack Watrous. A Cerenkov-like maser based on a metamaterial structure. *Plasma Science, IEEE Transactions on*, 38(6):1462–1465, 2010.

[19] Qiang Cheng, Wei Xiang Jiang, and Tie Jun Cui. Spatial power combination for omnidirectional radiation via anisotropic metamaterials. *Physical review letters*, 108(21):213903, 2012.

[20] Laszlo B Kish. End of Moore's law: thermal (noise) death of integration in micro and nano electronics. *Physics Letters A*, 305(34):144–149, December 2002.

[21] M. A. Olmstead, N. M. Amer, S. Kohn, D. Fournier, and A. C. Boccara. Photothermal displacement spectroscopy: An optical probe for solids and surfaces. *Applied Physics A*, 32(3):141–154, November 1983.

[22] H. A. Schuessler, S. H. Chen, Z. Rong, and Z. C. Tang. Surface absorption measurements of thin films by cavity-enhanced photothermal spectroscopy. *Optics Letters*, 16(8):608–610, April 1991.

[23] E. Welsch and D. Ristau. Photothermal measurements on optical thin films. *Applied Optics*, 34(31):7239–7253, November 1995.

[24] Mireille Commandr and Pierre Roche. Characterization of optical coatings by photothermaldeflection. *Applied Optics*, 35(25):5021–5034, September 1996.

[25] Nerijus Šiaulys, Laurent Gallais, and Andrius Melninkaitis. Direct holographic imaging of ultrafast laser damage process in thin films. *Optics Letters*, 39(7):2164, April 2014.

[26] Nicolaas Bloembergen. Laser-induced electric breakdown in solids. *IEEE Journal of Quantum Electronics*, 10(3):375–386, 1974.

[27] James R. Palmer. Continuous Wave Laser Damage On Optical Components. *Optical Engineering*, 22(4):224435, August 1983.

[28] Rashmi S. Shah, Justin J. Rey, and Alan F. Stewart. Limits of performance: CW laser damage. *Proceedings of the SPIE*, 6403:640305–640305, 2007.

[29] M. D. Perry, B. C. Stuart, P. S. Banks, M. D. Feit, V. Yanovsky, and A. M. Rubenchik. Ultrashort-pulse laser machining of dielectric materials. *Journal of Applied Physics*, 85(9):6803–6810, 1999.

[30] D. W. Fradin, N. Bloembergen, and J. P. Letellier. Dependence of laserinduced breakdown field strength on pulse duration. *Applied Physics Letters*, 22(12):635–637, June 1973.

[31] N. Bloembergen. Role of cracks, pores, and absorbing inclusions on laser induced damage threshold at surfaces of transparent dielectrics. *Applied optics*, 12(4):661–664, 1973.

[32] E. W. Van Stryland, M. J. Soileau, Arthur L. Smirl, and William E. Williams. Pulse-width and focal-volume dependence of laser-induced breakdown. *Physical Review B*, 23(5):2144–2151, March 1981.

[33] Jack H. Campbell, Frank Rainer, Mark R. Kozlowski, C. Robert Wolfe, Ian M. Thomas, and Fred P. Milanovich. Damage resistant optics for a megajoule solid state laser. volume 1441, pages 444–456, 1991.

[34] D. Du, X. Liu, G. Korn, J. Squier, and G. Mourou. Laser-induced breakdown by impact ionization in SiO2 with pulse widths from 7 ns to 150 fs. *Applied Physics Letters*, 64(23):3071–3073, June 1994.

[35] An-Chun Tien, Sterling Backus, Henry Kapteyn, Margaret Murnane, and Grard Mourou. Short-Pulse Laser Damage in Transparent Materials as a Function of Pulse Duration. *Physical Review Letters*, 82(19):3883–3886, May 1999.

[36] Arlee V. Smith and Binh T. Do. Bulk and surface laser damage of silica by picosecond and nanosecond pulses at 1064 nm. *Applied Optics*, 47(26):4812, September 2008.

[37] K. Olson, A. Ogloza, J. Thomas, and J. Talghader. High power laser heating of low absorption materials. *Journal of Applied Physics*, 116(12):123106, September 2014.

[38] R. M. Wood. Laser induced damage thresholds and laser safety levels. Do the units of measurement matter? *Optics & Laser Technology*, 29(8):517–522, April 1998.

[39] S. J. Mihailov, C. W. Smelser, D. Grobnic, R. B. Walker, Ping Lu, Huimin Ding, and J. Unruh. Bragg gratings written in all-SiO2 and Ge-doped core fibers with 800-nm femtosecond radiation and a phase mask. *Journal of Lightwave Technology*, 22(1):94–100, January 2004.

[40] Larry D. Merkle, N. Koumvakalis, and M. Bass. Laserinduced bulk damage in SiO2 at 1.064, 0.532, and 0.355 m. *Journal of Applied Physics*, 55(3):772–775, February 1984.

[41] Lucas N. Taylor, Andrew K. Brown, Aaron J. Pung, Eric G. Johnson, and Joseph J. Talghader. Continuous-wave laser damage of uniform and nanolaminate hafnia and titania optical coatings. *Optics Letters*, 38(21):4292–4295, November 2013.

[42] D. J. Richardson, J. Nilsson, and W. A. Clarkson. High power fiber lasers: current status and future perspectives [Invited]. *Journal of the Optical Society of America B*, 27(11):B63, November 2010.

[43] Tony Hoult. FIBER LASERS: Fiber-laser technology grows more diverse, December 2011.

[44] K. Yamakawa, M. Aoyama, S. Matsuoka, T. Kase, Y. Akahane, and H. Takuma. 100-TW sub-20-fs Ti:sapphire laser system operating at a 10-Hz repetition rate. *Optics Letters*, 23(18):1468, September 1998.

[45] M. Pittman, S. Ferr, J. P. Rousseau, L. Notebaert, J. P. Chambaret, and G. Chriaux. Design and characterization of a near-diffraction-limited femtosecond 100-TW 10-Hz high-intensity laser system. *Applied Physics B*, 74(6):529–535, April 2002.

[46] M. Aoyama, K. Yamakawa, Y. Akahane, J. Ma, N. Inoue, H. Ueda, and H. Kiriyama. 085-PW, 33-fs Ti:sapphire laser. *Optics Letters*, 28(17):1594, September 2003.

[47] Nicholas T. Gabriel and Joseph J. Talghader. Thermal conductivity and refractive index of hafnia-alumina nanolaminates. *Journal of Applied Physics*, 110(4):043526, 2011.

[48] M. L. Grilli, D. Ristau, M. Dieckmann, and U. Willamowski. Thermal conductivity of e-beam coatings. *Applied Physics A*, 71(1):71–76, July 2000.

[49] David G. Cahill and Thomas H. Allen. Thermal conductivity of sputtered and evaporated SiO2 and TiO2 optical coatings. *Applied Physics Letters*, 65(3):309–311, July 1994.

[50] M. Mero, J. Liu, W. Rudolph, D. Ristau, and K. Starke. Scaling laws of femtosecond laser pulse induced breakdown in oxide films. *Physical Review B*, 71(11):115109, March 2005.

[51] Scott C. Jones, Peter Braunlich, R. Thomas Casper, Xiao-An Shen, and Paul Kelly. Recent Progress On Laser-Induced Modifications And Intrinsic Bulk Damage Of Wide-Gap Optical Materials. *Optical Engineering*, 28(10):281039–281039–, 1989.

[52] Rafael R. Gattass and Eric Mazur. Femtosecond laser micromachining in transparent materials. *Nature Photonics*, 2(4):219–225, April 2008.

[53] B. C. Stuart, M. D. Feit, S. Herman, A. M. Rubenchik, B. W. Shore, and M. D. Perry. Nanosecond-to-femtosecond laser–induced breakdown in dielectrics. *Physical Review B*, 53(4):1749–1761, January 1996.

[54] Hernando Garcia. Tunneling assisted two-photon absorption: The nonlinear Franz-Keldysh effect. *Physical Review B*, 74(3):035212, July 2006.

[55] Vitali E. Gruzdev. Laser-induced ionization of solids: back to Keldysh. volume 5647, pages 480–492, 2005.

[56] John F. Ready. *Effects of High-Power Laser Radiation*. Academic Press, August 1971.

[57] Kyle David Olson. *High Power Continuous Wave Laser Heating and Damage with Contamination, and Non-Uniform Spectrally Dependent Thermal Photon Statistics*. Ph.D., University of Minnesota, United States – Minnesota, 2015.

[58] L. J. Shaw-Klein, S. J. Burns, and S. D. Jacobs. Model for laser damage dependence on thin-film morphology. *Applied Optics*, 32(21):3925, July 1993.

[59] J L Emmett, W F Krupke, and J B Trenholme. Future development of high-power solid-state laser systems. *Soviet Journal of Quantum Electronics*, 13(1):1–23, January 1983.

[60] W. F. Krupke, M. D. Shinn, J. E. Marion, J. A. Caird, and S. E. Stokowski. Spectroscopic, optical, and thermomechanical properties of neodymium- and chromium-doped gadolinium scandium gallium garnet. *Journal of the Optical Society of America B*, 3(1):102, January 1986.

[61] S. Albin, A. D. Cropper, L C. Watkins, Charles E. Bvvik, and A. M. Buoncristiani. Laser Damage Threshold Of Diamond Films. *Optical Engineering*, 28(3):283281–283281, 1989.

[62] Shuvendu Jena, Raj Bahadur Tokas, Nitin M. Kamble, Sudhakar Thakur, and Naba Kishore Sahoo. Optical properties and laser damage threshold of HfO_2SiO_2 mixed composite thin films. *Applied Optics*, 53(5):850, February 2014.

[63] Nicholas Theodore Gabriel. *High-power and high-aspect-ratio optical coatings by atomic layer deposition.* Ph.D., University of Minnesota, United States – Minnesota, 2011.

[64] Shiuh Chao, Wen-Hsiang Wang, Min-Yu Hsu, and Liang-Chu Wang. Characteristics of ion-beam-sputtered high-refractive-index TiO2-SiO2 mixed films. *Journal of the Optical Society of America A*, 16(6):1477–1483, June 1999.

[65] Ryo Tateno, Hajime Okada, Tomohito Otobe, Keigo Kawase, James K. Koga, Atsushi Kosuge, Keisuke Nagashima, Akira Sugiyama, and Kunihiro Kashiwagi. Negative effect of crystallization on the mechanism of laser damage in a HfO2/SiO2 multilayer. *Journal of Applied Physics*, 112(12):123103, 2012.

[66] David W. Fradin and Michael Bass. Electron avalanche breakdown induced by ruby laser light. *Applied Physics Letters*, 22(5):206–208, March 1973.

[67] D. W. Fradin, Eli Yablonovitch, and Michael Bass. Confirmation of an Electron Avalanche Causing Laser-induced Bulk Damage at 1.06 m. *Applied Optics*, 12(4):700–709, April 1973.

[68] M. J. Soileau and M. Bass. Laser-induced breakdown in crystalline and amorphous SiO2. *IEEE Journal of Quantum Electronics*, 16(8):814–814, 1980.

[69] D. W. Fradin and Michael Bass. Effects of lattice disorder on the intrinsic optical damage fields of solids. *Applied Physics Letters*, 23(11):604–606, December 1973.

[70] Jianhua Zhao, Xiangyang Li, Hua Liu, Runqing Jiang, Zhaopeng Liu, Zhihan Hu, Haimei Gong, and Jiaxiong Fang. Damage threshold of HgCdTe induced by continuous-wave CO2 laser. *Applied Physics Letters*, 74(8):1081–1083, February 1999.

[71] Haifeng Qi, Qingpu Wang, Xingyu Zhang, Zejin Liu, Zhaojun Liu, Jun Chang, Wei Xia, and Guofan Jin. Investigation on damage process of GaAs induced by 1064nm continuous laser. *Journal of Applied Physics*, 103(3):033106–033110, February 2008.

[72] Kwang Hyun Lee, Wan Soon Shin, and Eung Cheol Kang. Analysis of optical damage in germanium induced by a continuous wave laser. *Applied Optics*, 52(10):2055–2061, April 2013.

[73] Keith E. Puttick, Rune Holm, Detlev Ristau, Urs Natzschka, George Kiriakidis, Nirmal Garawal, Eddie Judd, David Holland, David Greening, Nick Ellis, Mark Wilkinson, Miguel Garcia Pamies, and Celestino Sanviti. Continuous-wave CO2-laser-induced damage thresholds in optical components. *Proceedings of the SPIE*, 3244:188–198, 1998.

[74] Hui Gong, Cheng F. Li, and Zhong Y. Li. CW-laser-induced thermal and mechanical damage in optical materials. *Proceedings of the SPIE*, 3578:576–583, 1999.

[75] Sangho S. Kim, Nicholas T. Gabriel, Wing S. Chan, and Joseph J. Talghader. Infrared absorption signature on laser-damaged optical thin films. *Optics Letters*, 34(14):2162–2164, July 2009.

[76] Shin-ichi Zaitsu, Shinji Motokoshi, Takahisa Jitsuno, Masahiro Nakatsuka, and Tatsuhiko Yamanaka. Laser Damage Properties of Optical Coatings with

Nanoscale Layers Grown by Atomic Layer Deposition. *Japanese Journal of Applied Physics*, 43(3):1034–1035, 2004.

[77] Dennis M. Hausmann and Roy G. Gordon. Surface morphology and crystallinity control in the atomic layer deposition (ALD) of hafnium and zirconium oxide thin films. *Journal of Crystal Growth*, 249(12):251–261, February 2003.

[78] Menelaos K. Poutous, Aaron J. Pung, Pradeep Srinivasan, Zachary A. Roth, and Eric G. Johnson. Polarization selective, graded-reflectivity resonance filter, using a space-varying, guided-mode resonance structure. *Optics Express*, 18(26):27764–27776, December 2010.

[79] Allan Rosencwaig and J. B. Willis. Photoacoustic study of laser damage in thin films. *Applied Physics Letters*, 36(8):667–669, April 1980.

[80] Todd W. Murray and James W. Wagner. Laser generation of acoustic waves in the ablative regime. *Journal of Applied Physics*, 85(4):2031–2040, February 1999.

[81] J.P Chen, X.W Ni, J Lu, and B.M Bian. Initial formation process of laser-induced plasma shock wave in air. *Optics Communications*, 176(46):437–440, April 2000.

[82] Jeffrey F. Herbstman, Alan J. Hunt, and Steven M. Yalisove. Morphologies and nonlinear scaling of laser damage on glass surfaces by tightly focused femtosecond pulses. *Applied Physics Letters*, 93(1):011112–011113, July 2008.

[83] Hongfei Jiao, Tao Ding, and Qian Zhang. Comparative study of Laser induce damage of HfO2/SiO2 and TiO2/SiO2 mirrors at 1064 nm. *Optics Express*, 19(5):4059–4066, February 2011.

[84] S.-M. Lee, David G. Cahill, and Thomas H. Allen. Thermal conductivity of sputtered oxide films. *Physical Review B*, 52(1):253–257, July 1995.

[85] R. Russel Austin, Raymond Michaud, Arthur H. Guenther, and Joseph Putman. Effects of Structure, Composition, and Stress on the Laser Damage Threshold of Homogeneous and Inhomogeneous Single Films and Multilayers. *Applied Optics*, 12(4):665–676, April 1973.

[86] D.R.G. Mitchell, D.J. Attard, K.S. Finnie, G. Triani, C.J. Barb, C. Depagne, and J.R. Bartlett. TEM and ellipsometry studies of nanolaminate oxide films prepared using atomic layer deposition. *Applied Surface Science*, 243(14):265–277, April 2005.

[87] R. Raghavan, M. Bechelany, M. Parlinska, D. Frey, W. M. Mook, A. Beyer, J. Michler, and I. Utke. Nanocrystalline-to-amorphous transition in nanolaminates grown by low temperature atomic layer deposition and related mechanical properties. *Applied Physics Letters*, 100(19):191912–191914, May 2012.

[88] Rolf Apetz and Michel P. B. van Bruggen. Transparent Alumina: A Light-Scattering Model. *Journal of the American Ceramic Society*, 86(3):480–486, March 2003.

[89] Hendrik Christoffel Hulst and H. C. van de Hulst. *Light Scattering by Small Particles*. Courier Corporation, 1957.

[90] H. S. Carslaw and J. C. Jaeger. *Conduction of Heat in Solids*. Oxford University Press, Oxford Oxfordshire : New York, 2 edition edition, April 1986.

[91] Lucas Taylor and Joseph Talghader. Monitoring and analysis of thermal deformation waves with a high-speed phase measurement system. *Applied Optics*, 54(30):9010–9016, October 2015.

[92] Avanish Kumar Dubey and Vinod Yadava. Laser beam machiningA review. *International Journal of Machine Tools and Manufacture*, 48(6):609–628, May 2008.

[93] P. Kwee, C. Bogan, K. Danzmann, M. Frede, H. Kim, P. King, J. Pld, O. Puncken, R. L. Savage, F. Seifert, P. Wessels, L. Winkelmann, and B. Willke. Stabilized high-power laser system for the gravitational wave detector advanced LIGO. *Optics Express*, 20(10):10617, May 2012.

[94] R. Kodama, P. A. Norreys, K. Mima, A. E. Dangor, R. G. Evans, H. Fujita, Y. Kitagawa, K. Krushelnick, T. Miyakoshi, N. Miyanaga, T. Norimatsu, S. J. Rose, T. Shozaki, K. Shigemori, A. Sunahara, M. Tampo, K. A. Tanaka, Y. Toyama, T. Yamanaka, and M. Zepf. Fast heating of ultrahigh-density plasma as a step towards laser fusion ignition. *Nature*, 412(6849):798–802, August 2001.

[95] J. Jasapara, A. V. V. Nampoothiri, W. Rudolph, D. Ristau, and K. Starke. Femtosecond laser pulse induced breakdown in dielectric thin films. *Physical Review B*, 63(4):045117, January 2001.

[96] M. C. Downer, R. L. Fork, and C. V. Shank. Femtosecond imaging of melting and evaporation at a photoexcited silicon surface. *Journal of the Optical Society of America B*, 2(4):595, April 1985.

[97] Stavros G. Demos, Rajesh N. Raman, and Raluca A. Negres. Time-resolved imaging of processes associated with exit-surface damage growth in fused silica following exposure to nanosecond laser pulses. *Optics Express*, 21(4):4875, February 2013.

[98] L. N. Taylor and J. J. Talghader. Ring-like damage morphologies produced by continuous-wave laser irradiation. In Gregory J. Exarhos, Vitaly E. Gruzdev, Joseph A. Menapace, Detlev Ristau, and Mj Soileau, editors, *Proceedings of the SPIE*, page 92371L, October 2014.

[99] T. Ikeda, G. Popescu, R. Dasari, and M. Feld. Hilbert phase microscopy for investigating fast dynamics in transparent systems. *Optics Letters*, 30(10):1165–1167, 2005.

[100] Miguel Arevallilo Herráez, David R. Burton, Michael J. Lalor, and Munther A. Gdeisat. Fast two-dimensional phase-unwrapping algorithm based on sorting by reliability following a noncontinuous path. *Applied Optics*, 41(35):7437–7444, December 2002.

[101] David J. Griffiths. *Introduction to Electrodynamics*. Addison-Wesley, Boston, 4 edition edition, October 2012.

[102] L. Prod'homme. A new approach to the thermal change in the refractive index of glasses. *Phys. Chem. Glasses*, 1(4):119, August 1960.

[103] A. R. Forouhi and I. Bloomer. Optical properties of crystalline semiconductors and dielectrics. *Physical Review B*, 38(3):1865–1874, July 1988.

[104] Fan Zhang, Rong-Jun Zhang, Dong-Xu Zhang, Zi-Yi Wang, Ji-Ping Xu, Yu-Xiang Zheng, Liang-Yao Chen, Ren-Zhong Huang, Yan Sun, Xin Chen, Xiang-Jian Meng, and Ning Dai. Temperature-Dependent Optical Properties of Titanium Oxide Thin Films Studied by Spectroscopic Ellipsometry. *Applied Physics Express*, 6(12):121101, December 2013.

[105] Toma Poar and Janez Moina. Measurement of Elastic Waves Induced by the Reflection of Light. *Physical Review Letters*, 111(18):185501, October 2013.

[106] M. L. Baesso, J. Shen, and R. D. Snook. Mode-mismatched thermal lens determination of temperature coefficient of optical path length in soda lime glass at different wavelengths. *Journal of Applied Physics*, 75(8):3732–3737, April 1994.

[107] Gorachand Ghosh. Model for the thermo-optic coefficients of some standard optical glasses. *Journal of Non-Crystalline Solids*, 189(12):191–196, August 1995.

[108] M. L. Baesso, J. Shen, and R. D. Snook. Modemismatched thermal lens determination of temperature coefficient of optical path length in soda lime glass at different wavelengths. *Journal of Applied Physics*, 75(8):3732–3737, April 1994.

[109] Lucas N. Taylor and Joseph J. Talghader. Subsampling phase retrieval for rapid thermal measurements of heated microstructures. *Optics Letters*, XX(XX):XXXX–XXXX, June 2016.

[110] C. A. DeVries and R. D. Mason. Subsampling Architecture for Low Power Receivers. *IEEE Transactions on Circuits and Systems II: Express Briefs*, 55(4):304–308, April 2008.

[111] J. Klzer, E. Oesterschulze, and G. Deboy. Thermal imaging and measurement techniques for electronic materials and devices. *Microelectronic Engineering*, 31(14):251–270, February 1996.

[112] W. Claeys, S. Dilhaire, V. Quintard, J. P. Dom, and Y. Danto. Thermoreflectance optical test probe for the measurement of current-induced temperature changes in microelectronic components. *Quality and Reliability Engineering International*, 9(4):303–308, July 1993.

[113] Franz Mayinger, editor. *Optical Measurements*. Springer Berlin Heidelberg, Berlin, Heidelberg, 1994.

[114] Taewoo Kim, Renjie Zhou, Lynford L. Goddard, and Gabriel Popescu. Solving inverse scattering problems in biological samples by quantitative phase imaging. *Laser & Photonics Reviews*, 10(1):13–39, January 2016.

[115] Mitsuo Takeda, Hideki Ina, and Seiji Kobayashi. Fourier-transform method of fringe-pattern analysis for computer-based topography and interferometry. *Journal of the Optical Society of America*, 72(1):156–160, January 1982.

[116] Takahiro Ikeda, Gabriel Popescu, Ramachandra R. Dasari, and Michael S. Feld. Hilbert phase microscopy for investigating fast dynamics in transparent systems. *Optics Letters*, 30(10):1165–1167, May 2005.

[117] Emilio Snchez-Ortiga, Pietro Ferraro, Manuel Martnez-Corral, Genaro Saavedra, and Ana Doblas. Digital holographic microscopy with pure-optical spherical phase compensation. *Journal of the Optical Society of America A*, 28(7):1410–1417, July 2011.

[118] Ana Doblas, Emilio Snchez-Ortiga, Manuel Martnez-Corral, Genaro Saavedra, Pedro Andrs, and Jorge Garcia-Sucerquia. Shift-variant digital holographic microscopy: inaccuracies in quantitative phase imaging. *Optics Letters*, 38(8):1352–1354, April 2013.

[119] Nelson Cardenas and Samarendra Mohanty. Decoupling of geometric thickness and refractive index in quantitative phase microscopy. *Optics Letters*, 38(6):1007–1009, March 2013.

[120] D. Gabor. A new microscopic principle. *Nature*, 161(4098):777–778, May 1948.

[121] J. W. Goodman and R. W. Lawrence. DIGITAL IMAGE FORMATION FROM ELECTRONICALLY DETECTED HOLOGRAMS. *Applied Physics Letters*, 11(3):77–79, August 1967.

[122] Giancarlo Pedrini, Wolfgang Osten, and Mikhail E. Gusev. High-speed digital holographic interferometry for vibration measurement. *Applied Optics*, 45(15):3456–3462, May 2006.